Polarization modulators for CMBPol

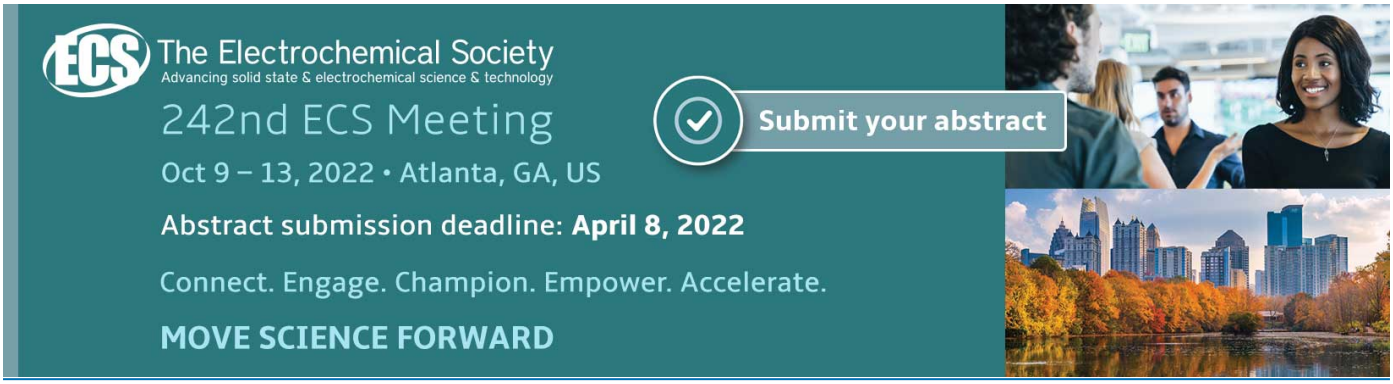

Journal of Physics: Conference Series **155** (2009) 012006 doi:10.1088/1742-6596/155/1/012006

Polarization Modulators for CMBPol

P A R Ade[1], David T Chuss[2], Shaul Hanany[3], V Haynes[4], Brian G. Keating[5], A. Kogut[6], John E. Ruhl[7], G Pisano[4], G Savini[1], and E J Wollack[8]

[1] Cardiff University, School of Physics and Astronomy, Queens Buildings, The Parade, Cardiff, CF24 3AA, UK
[2] NASA Goddard Space Flight Center, Code 665, Greenbelt, MD, 20771 USA
[3] School of Physics and Astronomy, University of Minnesota/Twin Cities, Minneapolis, MN, 55455, USA
[4] The University of Manchester, School of Physics and Astronomy - Alan Turing Building, Upper Brooke street, Manchester, M13 4PL, UK
[5] Department of Physics, University of California, San Diego, La Jolla, CA 92093-0424 USA
[6] Code 665 Goddard Space Flight Center, Greenbelt, MD 20771
[7] Physics Department, Case Western Reserve University, Cleveland, OH, 44106 USA
[8] Observational Cosmology Laboratory, NASA/GSFC, Greenbelt, MD 20771

Abstract.

We review a number of technologies that are candidates for active polarization modulators for CMBPol. The technologies are appropriate for instruments that use bolometric detectors and include birefringent crystal-based and metal-mesh-based half-wave plates, variable phase polarization modulator, Faraday rotator, and photolithographed modulators. We also give a current account of the status of millimeter-wave orthomode transducers.

1. Introduction

Shaul Hanany

School of Physics and Astronomy, University of Minnesota/Twin Cities, Minneapolis, MN, 55455, USA

E-mail: hanany@physics.umn.edu

The experimental technique of temporal modulation of amplitude, frequency or phase has long been a powerful technique to separate signals from sources of noise or from sources of systematic errors. In a generic amplitude modulation application the signal is modulated at a frequency f and then demodulated using phase-sensitive detection (either in hardware or in software) with a bandwidth Δf around the center frequency. Rejection of noise, or equivalently improved sensitivity, comes from moving the signal to high frequencies, away from typical $1/f$ noise sources in the experiment. Rejection of systematic errors comes from moving the signal to frequencies that do not contain contributions from specific systematic effects.

The cosmic microwave background's B-mode polarization is expected to have an RMS magnitude that is smaller than 100 nK. This magnitude is at least a factor of $\sim$10 smaller than the E-mode signal, a factor of $\sim$100 smaller than the temperature anisotropy, and a factor

of $\sim 10^7$ smaller than the temperature of the CMB itself. The smallness of the signal requires high sensitivity and exquisite control of polarimetric systematics. Temporal modulation of the incident polarization can provide improved sensitivity and rejection of systematics errors, hence the interest in polarization modulation for future CMB polarization experiments, as well as for CMBPol.

This paper discusses a number of polarization modulation techniques that are technology candidates for CMBPol. Since the TFCR report [1] has endorsed a bolometric detector technology for the satellite, this paper will concentrate only on polarization modulation techniques for bolometric experiments. It is broadly expected that the scan pattern of CMBPol will be optimized for polarization measurements.

There is no evidence yet that it is imperative that CMBPol will have an active polarization modulator. A number of experiments have already made detections of the E-mode polarization without employing such modulator [2, 3]. The term 'active' is used here to denote a specific hardware implementation inside the instrument that is meant to switch polarization states, as opposed to modulation only through the scan pattern across the sky. MAXIPOL [4] was the first experiment to measure the polarization of the CMB with an active modulator, which was a combination of a rotating half wave plate and a stationary grid. The lessons learned from these experiments were discussed in a separate workshop dedicated to discussion of systematic errors from polarization experiments. Our goal in this paper is to survey candidate active polarization modulation approaches from a technical point of view. The question of whether such modulation is necessary for CMBPol is outside the scope of this paper.

It is useful to enumerate the properties of an ideal polarization modulator. The different technologies that will be described in subsequent chapters address some of these properties well, while falling short with others. This is the inevitable trade-off that the experimental designer must consider.

- An ideal modulator should be the first element in the optical train of the instrument. In this way it modulates only the incident polarization from sky sources; not any spurious polarization that is created by the instrument.
- An ideal modulator should modulate the polarization on time scales that are fast compared to 1/f noise contributions to the measurement.
- An ideal modulator must have high modulation efficiency. In other words, an ideal modulator should not decrease the level of polarization of the incident signal.
- Almost all modulation techniques give rise to spurious signals that are synchronous with the modulation. Such spurious signals can be induced by a number of sources including mechanical vibrations, EMI, scattering, or modulation of transmission, to name just a few. An ideal modulator addresses potential sources of systematic effects, while not inducing systematic effects of its own.
- An ideal modulator is easy to fabricate, easy to implement mechanically, electrically and cryogenically, it does not produce significant power dissipation, and has low mass.

The technologies discussed in subsequent chapters were selected out of a wider array of possibilities because they are currently or have recently been actively pursued by a number of groups carrying out CMB polarization experiments. Section 2 discusses the use of a birefringent half wave plate made of crystalline material. The technique has substantial heritage in astronomy and has already been used in an experiment that reported CMB measurements [4]. Sections 3 and 4 discuss technologies that also have past heritage in millimeter-wave astronomy. However, no detection of CMB signals is yet reported with either. Both technologies are integrated into experiments that have recently searched, or will search in the near future, for the polarization of the CMB. In Section 5 the authors present a novel approach whereby standard metal-mesh filtering technology is extended to form a metal-mesh-based birefringent half-wave plate. A

prototype has been constructed and there are plans to make the first astronomical observations in the near future. Section 6 reviews the status of polarization modulators that are fabricated photolithographically on a silicon wafer. This technology is in relative infancy. There are no instruments yet operating with photolithographic modulators. The last section in this compilation discusses the status of ortho-mode transducers. Although these are not polarization modulators, we include the section because the review of the technology might be useful for designers of future polarization instruments.

All-in-all the goal of this paper to inform the choice of a polarization modulator for a future CMBPol mission.

2. Half Wave Plate Modulator

John E Ruhl
Physics Department, Case Western Reserve University, Cleveland, OH, 44106 USA
E-mail: ruhl@case.edu

Abstract. Polarization modulators that are based on the introduction of a quasioptical phase delay between two orthogonal linear polarizations are reviewed. The general principle behind the device and the application to the Beyond Einstein Inflation Probe are addressed.

2.1. Introduction

The birefringent halfwave plate (HWP) polarization modulator, while new to the CMB field, has been used for decades at shorter wavelengths. The basic idea is simple; a polarized plane wave passing through a HWP will have its polarization orientation rotated by $\Delta\psi = 2\theta$, where θ is the angle between the incident polarization and one of the optical crystal axes. Rotating a HWP in front of a linearly polarized detector rotates the polarization sensitivity of that detector on the sky, nominally without affecting its beam pattern. This virtue, rotating polarization sensitivity without rotating a potentially asymmetric beam, is the main reason many upcoming CMB polarimeters (including ACT, ABS, Bicep2/Spud, Clover, EBEX, Polarbear, and Spider) will use birefringent sapphire HWP polarization modulators.

Maxipol [5, 6] is the only experiment so far to publish CMB observations using a HWP polarization modulator. With a single night of data from a balloon platform, the sensitivity was insufficient to probe B-modes, but was a good demonstration of using a HWP modulator to measure polarization on the sky.

The future use of HWPs for B-mode polarization observations will test a variety of designs and strategies for using these devices. Here we review some of the issues associated with using HWPs, and the ongoing work that will test these devices in future CMB polarization observations.

2.2. Major design and observing choices

There are three major design choices that each HWP implementation must make: bandwidth, operation temperature, and rotation style (continuous or stepped).

The optical design of the HWP is driven by desired bandwidth. Some experiments will use separate optical paths for each observing band, with a separate HWP optimized for each. For these, the required fractional bandwidth is of order 25%. Other experiments put the HWP in an optical path that is shared by several bands; in this case, the required fractional bandwidth is much larger, of order unity. In practice, the single-band design can be simpler, using only a single-layer birefringent crystal and a single-layer anti-reflection coating. Multi-band designs require a stack of multiple birefringent plates with multilayer anti-reflection coatings. Of course all optical designs must also respect the upper limit on available diameter of materials used to construct the HWP; birefringent sapphire is available in diameters up to at least 330mm.

Most upcoming experiments are baselining cryogenic HWPs, which ensures very low thermal emission from the HWP in the observing bands and minimizes signals from reflections. However, even at 300 K the in-band emission of a single-plate sapphire HWP design is only about 2 K at 150 GHz, so ground-based experiments may be able to use ambient temperature HWPs. ACT has investigated such ambient-temperature operation [7]. The mm-wave loss in sapphire drops dramatically with temperature, so loading is unlikely to be an issue for any instrument (including CMBPol) using a cryogenic HWP.

HWPs can be used to separate beam asymmetries from polarization signals by occasional stepping of the HWP orientation or by continuously rotating it. The choice between these two strategies is intimately linked with the observing scan pattern and detector noise properties. This choice drives the mechanical design; stepper motors and conventional bearings are a good match to occasional stepping, while low heat dissipation requirements at cryogenic temperatures makes a passive magnetic bearing attractive, though perhaps not essential, for continuous rotation.

Continuous rotation comes in two flavors, which color the way one views the optical design criteria. The simplest use of a continuous rotation is to ensure the HWP modulates the polarization (at four times the HWP rotation rate f) very fast compared to rate at which the instrument's beam response is scanned across the sky. For such fast modulation, one can just lock in to the $4f$ component of the timestream and ignore other harmonics. Alternatively, one can scan across the sky fast compared to $4f$; in terms of analysis, this is much like a very rapid stepping of the waveplate.

2.3. Optical Designs and characterization

The coupling from a given input polarized signal to a polarized detector, as a function of photon frequency and HWP angle, can be calculated using E and H field boundary matching at each dielectric interface. An unpolarized version of this matching is worked out in matrix formulation in [8], while a polarized version is discussed in [9]. It is worth considering a few simple single-plate cases, however, to build intuition.

Case 1: When the input polarization is aligned with one of the crystal axes and the detector polarization sensitivity, the polarization is not rotated by the HWP at *any* photon frequency ν. Reflections at the various dielectric interfaces, however, will affect the transmission amplitude as a function of ν.

Case 2: Rotate the detector polarization sensitivity by 90° from Case 1. Again, the HWP does not rotate the input polarization at any ν; since the sky signal and detector sensitivity (assumed to have no crosspolar response) are crossed, there is no detector response at *any* ν. This is independent of reflections, since zero times anything is zero.

Case 3: Start with Case 1, but rotate the HWP by $\theta = 45°$. At the design frequency, the input polarization is rotated by exactly $\gamma = 2\theta = 90°$, so the detector response is zero. However, at other photon frequencies γ is not exactly 90°, so there is some detector response. This means that when the sky signal and detector sensitivity are aligned, rotating the HWP takes the band averaged signal from some large value (Case 1) to some small but non-zero value (Case 3).

Case 4: Start with Case 2, but rotate the HWP by $\theta = 45°$. At the design frequency, the input polarization is rotated by exactly $\gamma = 2\theta = 90°$, so the detector response is maximized. At nearby photon frequencies γ is not exactly 90°, so detector response is not maximized but it will still be large. This means that when the sky signal and detector sensitivity are orthogonal, rotating the HWP takes the band averaged signal from zero (Case 2) to some large value (Case 4).

Full calculations of the coupling as a function of HWP orientation angle, for normal incidence and ideal materials, generally give signals that contain a DC level, a second harmonic of the HWP rotation frequency f, and the expected signal at $4f$, the amplitudes of which are a function of photon frequency. The $2f$ signal is the result of reflections that depend on how the input signal is aligned with the crystalline axes. A figure of merit called the "polarization modulation efficiency", particularly relevant to experiments using rapidly rotating HWPs, is unfortunately defined in different ways by different authors so we will avoid that terminology here.

The importance of various optical characteristics are driven by the desired bandwidth and

the mode of operation (stepped or slow rotation vs. fast rotation). In the fast-rotation case, the $4f$ signal amplitude and phase (as a function of ν across the band) are the major parameters of interest. In the slow-rotation and stepped modes, one needs to consider the spectral response as a function of input (sky) polarization angle, for each orientation of detector sensitivity and HWP rotation angle that will be used.

2.3.1. Single-plate designs A HWP constructed from a single slab of birefringent sapphire with a single-layer quarter-wave antireflection coating has a very large and uniform $4f$ signal across a 25% fractional bandwidth (top panel of Figure 1). The $2f$ signal, due to differential reflections when the input signal is aligned with the two crystal axes, is small; the DC signal is nearly the same as the $4f$ signal, indicating that the signal minima (dominated by DC + $4f$) are nearly zero. Note the absence of a $2f$ signal in the perpendicular case (Case #2 above); for the same reason, the signal minima area exactly zero, which means that the DC offset is equal to the $4f$ signal amplitude.

Several groups are building single-band, single-plate HWP systems that will be used in upcoming experiments. Our group at Case is constructing sets for Bicep2/SPUD and Spider, centered at 90, 145, 220, and 270GHz, each with about 25% fractional bandwidth. ACT, ABS, and Polarbear plan to use single-band, single-plate designs at 150 GHz in their first incarnations [7, 10, 11].

As Figure 1 illustrates, the HWP introduces features into the $4f$ amplitude bandpass of the system. These $4f$ features are independent of detector orientation relative to the sky signal, which means this can be treated just like another multiplicative effect defining the detector bandpass - there is no extra complication.

However, the $2f$ and *DC* features are not independent of detector orientation. For slow continuous HWP rotation, or stepped rotation, these effects must be accounted for. Figure 2 shows how this same HWP design affects sky-to-detector coupling depending on the relative angles of the sky signal, detector orientation, and HWP, for two orientations of sky signal and detector (coaligned and crossed) and four HWP orientations. The important thing to note is that in general a crossed detector pair with otherwise identical bands will have different frequency response to the same polarized sky signal. This is an extra complication that must be accounted for in the data analysis.

2.3.2. Multi-plate designs Multiple birefringent plates can be combined to significantly increase the useful bandwidth of the HWP [12, 13, 14]; these must be combined with wide-bandwidth anti-reflection coating to get good overall performance over a wide range of photon frequencies.

As an example, the calculated performance of representative a 3-plate design with a 5-layer AR coat is shown in Figure 3; with the $4f$ amplitude nearer to unity over a much larger range of photon frequencies than the single-plate design, this system enables optical designs where multiple bands share a single HWP.

Several groups are implementing multi-plate designs; Clover and EBEX are baselining them for their first observations, while other groups are considering them for use when they implement multiple bands in the future.

2.3.3. Characterization While many experiments are planning to implement HWPs into their B-mode CMB observing instruments in the near future, there has been only a relatively small amount of detailed optical testing published so far.

The only published CMB observations with a HWP were done by Maxipol [6]. That system used a single birefringent sapphire plate and single-layer AR coat, optimized for its 150 GHz observing band. Significant offsets at the HWP rotation frequency and harmonics were caused by the drive system [15], which incorporated a G10 shaft attached to the center of the HWP and

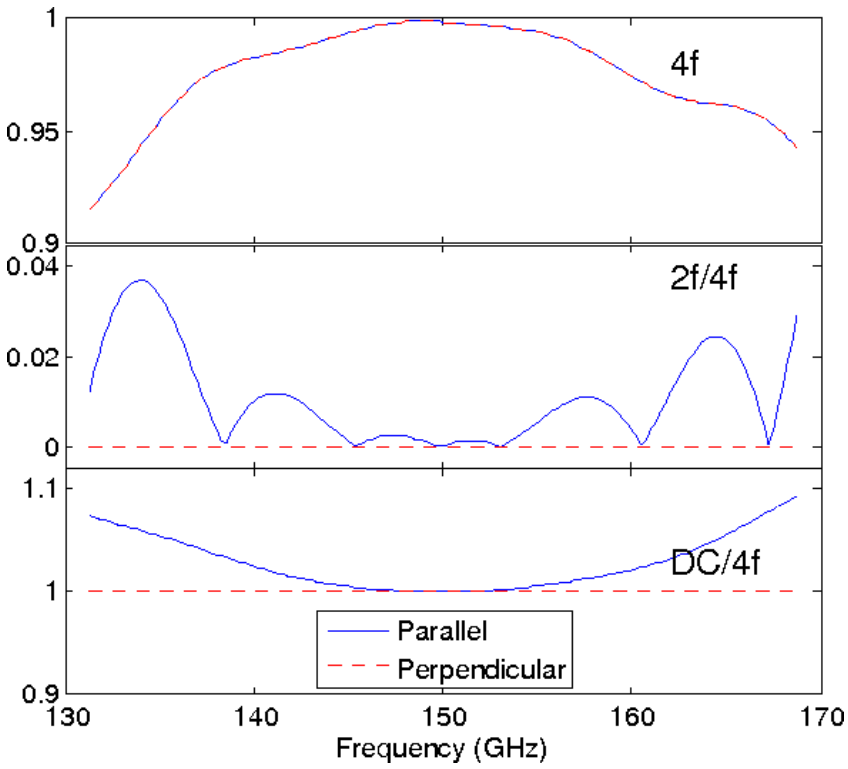

Figure 1. Calculated transmission signals from a completely polarized input, coupling into detectors that are sensitive to polarization parallel to (solid blue line) and perpendicular to (dashed red line) the input polarization. The top panel shows the signal that is modulated four times per HWP rotation ($4f$ component), which is the same for both plotted cases; the middle shows the ratio of the $2f$ to $4f$ (which is zero for the perpendicular case), and the bottom panel shows the ratio of the DC to $4f$, which is unity for the perpendicular case. The plotted points cover a 25% fractional bandwidth centered on 150GHz, using a single lossless sapphire waveplate ($n_s = 3.4$, $n_f = 3.07$) with an "ideal" quarter-wave AR coat that has an index $n_{AR} = \sqrt{(n_s + n_f)/2}$.

therefore within the optical path. Despite that issue (which future implementations of HWPs for CMB observations are all avoiding), the optical performance was sufficiently good to reconstruct sky maps at the detector sensitivity limit with no obvious systematics.

The ACT team [7] tested an ambient temperature HWP (again, single sapphire plate with a single layer AR coat) briefly installed on the CCAM instrument in Chile. Only a small amount of data was taken, but the optical performance was again promising.

Laboratory optical testing has included very narrow-band measurements using coherent sources and broadband FTS testing [13, 14]. To a large extent, this work has confirmed expectations, and has not yet raised any serious unexpected issues.

However, these tests have not yet probed all the relevant questions, such as whether spurious signals (eg from reflections) will be stable enough to avoid signal contamination, whether non-uniformities will induce systematics or degrade performance, and whether the frequency response can be characterized well enough to avoid limiting foreground subtraction. The importance of these issues is as much a function of the rest of the optical and detector system, and of the scan strategy, as they are of the HWP. We will learn an enormous amount from upcoming

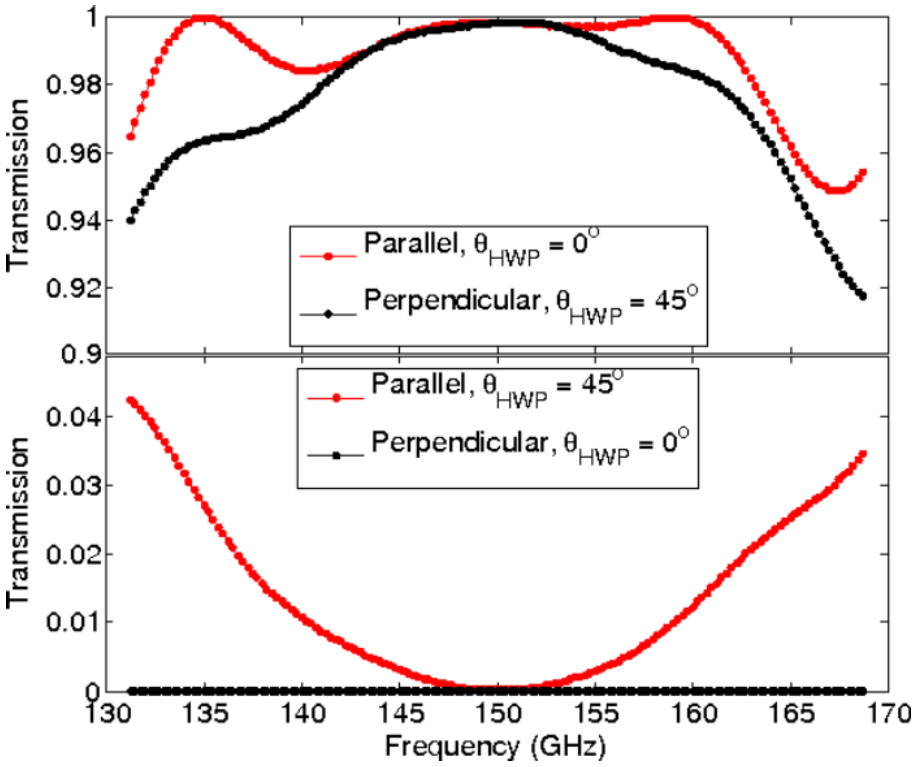

Figure 2. Calculated transmission as a function of photon frequency for detectors parallel (black symbols and lines) and perpendicular (red symbols and lines) to the incident polarization direction, for HWP orientations that nominally maximize (upper panel) and minimize (lower panel) those couplings. The HWP characteristics are the same as for Figure 1.

observations.

2.3.4. Cryogenic rotation schemes To be useful, a HWP must be rotated (continuously or stepped) during or between observations. If the waveplate is used at 300K (as is being investigated by the ACT team), such rotation and encoding of the HWP angular position is straightforward. Rotating at cryogenic temperatures, and knowing the HWP angular position to the required level of $\approx 0.1^\circ$, is another technical challenge that must be dealt with.

2.3.5. Stepped rotation Cryogenic stepped rotation is conceptually straightforward, with the caveat that linear thermal contractions must be handled. Several groups have used stepper motors at 4K to drive such motion; options range from commercially available cryo-vacuum stepper motors to simple modifications of motors built for room temperature operation. Incremental cryogenic encoders with the required precision have been constructed using cryogenic lasers, LED's, and photodiodes, and tested in the lab.

The large optical throughput of CMB polarimeters is driving a desire for larger diameter HWP's than have been used before - as large as $\sim$ 30cm clear diameter. These large diameters increase the likelihood of failure of the large diameter ball bearing assemblies (with I.D. equal to or greater than the clear aperture) used by previous designs [16] as they thermally contract. We have built a design that avoids this problem by using three small rollers rather than one large bearing, which minimizes the likelihood of binding due to thermal contraction mismatches.

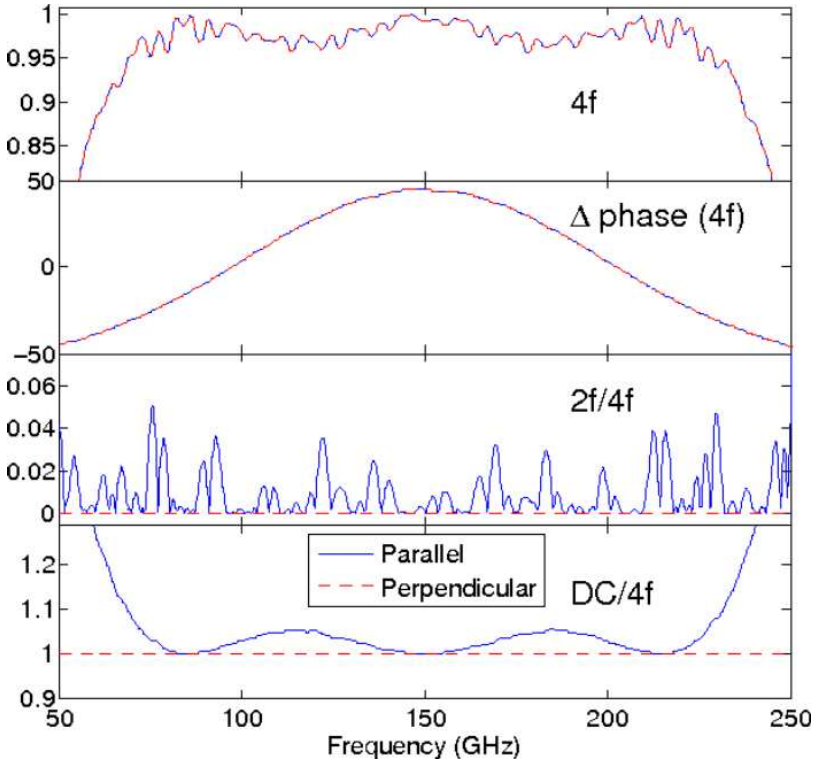

Figure 3. Similar to Figure 1, but for an example HWP system constructed from three birefringent sapphire plates (the middle layer is rotated by 50° with respect to the outer two layers, in this case) with a 5-layer AR coat. Here we have added another panel to the plot to show the phase difference of the $4f$ signal as a function of photon frequency, which limits the useful width of individual bands using this HWP; that is, the HWP system is still very good for multiple (narrow) bands within the frequency limits shown, but is loses efficiency for very wide bands. The reflections at the internal and external interfaces create a rich set of features in the $4f$ and $2f$ amplitudes as a function of photon frequency.

2.3.6. Continuous rotation Cryogenic continuous rotation raises the issues of microphonic noise and the generation of excessive heat at those temperatures. Passive superconducting magnetic bearings (SMBs) [17] have very low friction, and therefore minimize both microphonics and heating. Polarbear, however, will be using a standard ball-bearing at 50K, where the heat loading is less of an issue [11].

Several drives have been developed for cryogenic, continuously rotating HWPs; EBEX will be using a magnetically levitated HWP, driven by a brushless DC motor outside the cryostat, coupled to the HWP by a shaft and a belt [18, 19]. Polarbear is baselining a similar drive, but using standard ball bearings at the 50K HWP [11]. Here at Case, we have also prototyped and tested an integrated synchronous AC motor built into the rotor, riding on a SMB.

Knowledge of the rotation angle is of course key; as with stepped systems, encoders based on cryogenic lasers, LED's and photodiodes should provide the required precision.

2.4. Future Development Work

A large number of of upcoming CMB polarization experiments (eg ABS, ACT, Bicep2/SPUD, Clover, EBEX, Polarbear, and Spider) are planning to use birefringent crystal HWPs. Calculations and preliminary testing indicate that HWPs should work well for these observations.

These experiments will test a wide variety of optical designs and rotation schemes, exactly as is needed to explore the usefulness of HWP polarization modulators for CMBPol.

After these upcoming experiments are done, the various HWP implementations used would be at TRL 7, defined as "System prototyping demonstration in an operational environment (ground or space)." Right now they are around TRL 4, "Component/subsystem validation in laboratory environment". The real question for CMBPol is whether it will be using a HWP very similar to those implemented in the upcoming generation of experiments, or will require modifications; given the newness of HWPs in CMB instruments and the differences between the suborbital and orbital environments, the need for some evolution is quite likely. For this reason, it would be good to support efforts to further develop HWP concepts that specifically target issues important for their actual use in CMBPol, above and beyond the existing suborbital experiments.

Journal of Physics: Conference Series **155** (2009) 012006 doi:10.1088/1742-6596/155/1/012006

3. Faraday Rotation Modulators for mm-Wavelength Polarimetry

Brian G Keating

Department of Physics, University of California, San Diego, La Jolla, CA 92093-0424 USA

E-mail: bkeating@ucsd.edu

Abstract. The design and performance of wide bandwidth linear polarization modulators based on the Faraday effect in corrugated cylindrical waveguide is described. The device can be used as a polarization modulator for millimeter-wave and microwave polarimetry and is functionally similar to a birefringent crystal waveplate, but with no moving parts. The Faraday rotation modulator's intrinsically single-moded design results in wide-bandwidth performance with low-loss, and is capable of polarization modulation up to ~ 10 kHz. The Faraday Rotation Modulator is capable of operation at cryogenic temperatures and is scalable for use up to electromagnetic frequencies of 300 GHz. Faraday rotation modulators operating at 100 and 150 GHz, with 30% fractional bandwidths in each band have been used to make astronomical observations of polarized galactic emission.

3.1. Introduction and Motivation

Measurements of the polarization of the cosmic microwave background (CMB) have the promise to revolutionize our understanding of the early universe. Unlike the temperature anisotropy of the CMB, which has been measured to exquisite precision over a wide range of angular scales, the polarization of the CMB has only recently been detected and remains relatively unexplored. To detect the faint CMB polarization it will also be necessary to detect and remove polarized galactic emission from interstellar dust and synchrotron sources which can be accomplished if polarimetry is done in multiple millimeter-wave bands.

Polarimeters often employ mechanisms to modulate the plane of polarization of the incident radiation field about the optical axis. In conjunction with an analyzer (to decompose the radiation into orthogonal polarization states), a modulator is used to exchange the polarized intensity between the two detectors (or two orientations of a single detector). If the modulation is done rapidly enough, this technique mitigates the effects of detector gain instability. If the detector's gain instability systematics are mitigated by other means, e.g. spatial scanning, then the FRM can be used in a "point-and-integrate" mode where it is used solely to modulate polarization. This can simplify either the optics, detectors (allowing for only one linear polarization state to be detected) or the telescope's mount. In such situations, having both FRM and scanning modulation, allow the tasks of beam systematics mitigation and detector fluctuation systematics mitigation to be separated.

3.1.1. Polarization modulation Traditionally, polarization modulation for millimeter-wave polarimeters was accomplished by physical rotation of the polarimeter about the optical axis [20, 21], mechanical rotation of a waveguide polarizer [22], rotation of a wire grid polarizer [23], or rotation of a birefringent half-waveplate [24, 25]. In many CMB experiments, polarization modulation is often effected by parallactic angle rotation ("sky rotation") with respect to the instrument coordinate system.

Classical polarization modulation mechanisms often employ bulky and complex mechanisms which are subject to failure with repeated use. The modulators described in this paper represent a novel approach to the technology of CMB polarization modulation. Early CMB polarimeters (including Penzias and Wilson's, which *was* polarization-sensitive) used a combination of sky-rotation with rotation of the entire telescope to modulate CMB polarization. These experiments

[26, 27] rotated hundreds or thousands of kilograms, were susceptible to vibration induced microphonic noise, and were limited mechanically to modulation rates < 0.1 Hz.

The next polarization modulation innovation was a birefringent half-waveplate: a single crystal of anisotropic dielectric (typically quartz or sapphire) that phase-delays one of the two linear polarizations [23, 5]. While the fragile ~ 1 kg, cryogenically-cooled crystal *can* be rotated at ~ 10 Hz with lower-vibration than rotation of the entire telescope, such a mechanism is prone to failure since bearing operation is a severe challenge at cryogenic temperatures. And since bolometers are sensitive to power dissipation at the 10^{-17}W level, even minute mechanical vibrations produced by the bearings are intolerable.

The Faraday Rotation Modulator[1] (FRM) shown in Figure 4, requires only "rotating" electrons (the generation of a solenoidal magnetic field) in a magnetized dielectric to effect polarization rotation. Therefore, FRMs reduce the rotating mass that provides modulation by 30 orders of magnitude! Furthermore, these devices are capable of rotating polarized millimeter wave radiation at rates up to 10 kHz—faster than any conceivable time-varying temperature- or optical-gain fluctuation. A superconducting NbTi solenoid wound around the waveguide provides the magnetic field that drives the ferrite into saturation, alternately parallel and anti-parallel to the propagation direction of the incoming radiation. The FRM rotates the CMB polarization vectors by $\pm 45^\circ$ at 1 Hz, well above 1/f-fluctuation timescales (caused by, for example, temperature variations). The Polarization Sensitive Bolometer (PSB) signals are detected using phase-sensitive amplification phase-referenced to the solenoidal field drive waveform.

Faraday Rotation Modulators, like waveplates, have the promise to mitigate optical systematic effects occurring "downstream" from the modulator. Though the FRMs described in this work operate in waveguide, following the primary aperture of the telescope and additional coupling optics, nevertheless the Faraday effect could also be able to be implemented in free-space, perhaps at a cold optical stop. In such an implementation the polarization modulation would be identical to a birefringent waveplate, except that *no* mechanical rotation mechanism would be required.

In free space, or in waveguide, Faraday modulation of the plane of polarization can be effected in a continuous modulation mode or in a step-and-integrate mode. In either mode the effective polarization angle can be commanded with extremely high precision and repeatability which also obviates the need for a servo system as used in a conventional half waveplate modulation.

The Faraday effect in waveguide has also been used to rotate millimeter-wave polarization between two fixed states -90° and $+90^\circ$. Such a mode is equivalent to a 180° phase switch. This implementation has been successfully deployed in the MBI experiment and is further described in this volume [28].

In November 2005 a millimeter-wave polarimeter with 49 spatial pixels was deployed to the United States' Amundsen-Scott South Pole Station. This CMB polarimeter called BICEP[27, 21] required low-systematic, high-reliability, polarization modulation. This led to development and observations with the FRMs as a secondary form of polarization modulation (the primary modulation mechanism being rotation of the BICEP telescope about its boresight axis).

The FRM provides rapid modulation of the plane of linear polarization (the dominant type of CMB polarization) and was operated in a continuously switching mode (as opposed to a continuously rotating mode or a "point-and-integrate mode"). In the continuously switching mode the Stokes parameter measured by a paid of linearly polarized detectors is switched between +Q and -Q. Only the polarized component of the incident flux is modulated and subsequently analyzed with phase-sensitive detection (lock-in amplification). In the BICEP experiment six FRMs; three operating at 100 GHz and three at 150 GHz, were deployed as

[1] US Patent Pending: "Wide Bandwidth Polarization Modulator, Switch, and Variable Attenuator," US Patent and Trademark Office, Serial Number: 60/689,740 (2005)

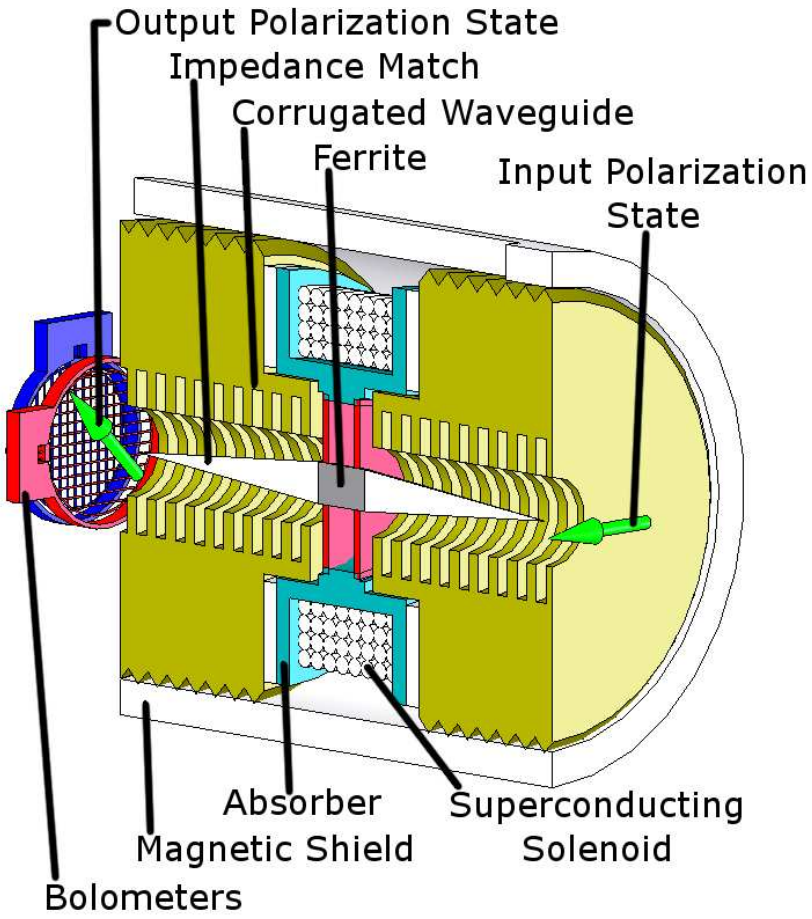

Figure 4. A cross-sectional view of a Faraday Rotation Modulator (FRM) pixel. Polarized light enters from the right, is rotated by $\pm 45^\circ$ and then analyzed (decomposed into orthogonal polarization components, which are detected individually by the polarization-sensitive bolometers, or PSBs). For each FRM pixel, the PSBs are contained within a corrugated feedhorn, cooled to 0.25 K, located approximately 20 cm from the FRM, which is placed in a corrugated waveguide at the interface between two corrugated feedhorns, placed back-to-back and cooled to 4 K – see Figure 5. The (schematic) location of the PSBs in this figure serves to illustrate the coordinate system used as the polarization basis. Figure credit: Thomas Renbarger.

a proof-of-concept test of the FRM technique and to explore operational modes for this new device. Preliminary results from BICEP's FRMs are discussed below.

In the 1970's a polarimeter which used a Faraday modulator and an orthomode transducer as a polarization analyzer was employed by Nanos [29] to conduct early studies observations of the CMB. The modulator described in this white paper (Fig. 4 has a bandwidth $\simeq$ 30 times greater than Nanos' or those currently available from commercial vendors such as MPI/QuinStar Technology Inc. Our devices are also capable of operation at cryogenic temperatures, which is an operational advantage not enjoyed by Nanos' devices nor commercially available devices.

3.2. Design

The magneto-optical design of the modulator is based on a room temperature isolator employing a ferrite dielectric waveguide [30] and a cryogenic isolator [31]. These isolators operate in

rectangular waveguide allowing precise mode filtration and low spurious mode generation. Operation as a polarization modulator requires matching modal propagation coefficients of the propagating modes in the entrance waveguide (TE_{10}, TE_{11}°, or HE_{11}°) and the propagating HE_{11}^{diel} mode in the dielectric guide. For the tests described in this paper a corrugated circular waveguide with a 2.35 mm diameter was used. The Faraday modulator design is displayed in Fig. 4.

To achieve magnetic saturation with low Joule heating, a solenoid constructed of superconducting copper niobium wire is used. According to the manufacturer of the ferrite this material has a saturation magnetization of $4\pi M_z = 5000$ gauss which is obtained with an applied magnetic field of $H \simeq 30$ Oe. This field is produced by the superconducting solenoid with $N \simeq 200$ amp-turns. The calculated self inductance of the solenoid is $L = \mu_o N^2 A/\ell = 10$ mH where A and ℓ are the area and length of the solenoid. This value agrees well with the inductance measured with an LCR meter and directly by observing the L/R time constant of the solenoid at 4 K. All performance attributes of the modulator are improved with careful attention to assembly details and tolerances. In particular, the alumina cone-ferrite cylinder "toothpick" assembly must be placed along the propagation direction with less than 1° tilt, otherwise resonant mode conversion produces several dB of insertion loss.

3.2.1. Polarimetry with Faraday Rotation Modulators Figure 5 is a schematic illustration of a FRM as implemented in a bolometric polarimeter. Bolometric polarimeters, such as BICEP[21]

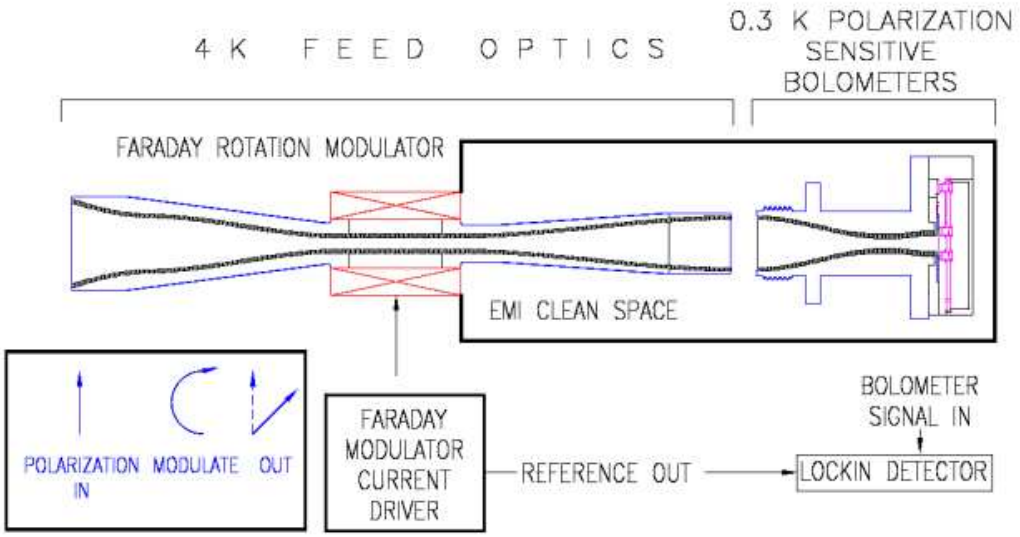

Figure 5. Conceptual schematic of a Faraday polarization modulator coupled to a polarization sensitive bolometer (PSB) used as a polarimeter. The modulator is placed at the waveguide choke and rotates the plane of linear polarization of the propagating HE^{11} spatial mode.

often utilize a back-to-back corrugated feedhorn geometry to provide (electromagnetic interference) EMI shielding between the beam-defining optics (typically cooled to $\simeq 4.2$ K)and the detector coupling optics (typically < 0.3 K). The EMI shield is implemented as a high-pass filter (waveguide choke) between the two back-to-back feedhorns in the beam-defining optics section, preventing radio frequency radiation from being detected by the high-impedance bolometers. The waveguide choke allows a single waveguide mode to propagate, and it is here that the FRM is installed.

Detection after modulation can be accomplished with a bolometric or HEMT amplifier radiometer. For the latter application, the rapid modulation frequencies available with the Faraday rotator allows the radiometer to be Dicke-switched in total power mode, *i.e.*without other forms of phase modulation. The FRM polarimeter, whether used with a HEMT amplifier or bolometer detector system, completely characterizes the linear polarization state of the incident radiation from the same spatial pixel in the focal plane of a telescope. This allows the incident radiation in each linear polarization state to propagate through the same optical train (windows, lenses, filters, detectors), under identical optical loading conditions. Unlike polarization modulation by physical rotation of the polarimeter, polarimeters employing FRMs allow the polarization to be modulated without moving the telescope's antenna beam on the sky. By keeping the spatial beam pattern fixed on the sky we isolate the polarization properties and can ignore variations of the beam response or excess variable pickup from the ground.

We used a pair of polarization sensitive bolometers (PSBs) to simultaneously analyze (separate the incident beam into orthogonal polarization states) and detect the power in each state [32]. For an incident electric field described by

$$\begin{aligned}\overrightarrow{E}(x,y,z,t) &= E_x(t)\sin\left[2\pi\left(\frac{z}{\lambda}-\nu t\right)+\phi_x(t)\right]\hat{\mathbf{x}} \\ &\quad +E_y(t)\sin\left[2\pi\left(\frac{z}{\lambda}-\nu t\right)+\phi_y(t)\right]\hat{\mathbf{y}}, \end{aligned} \tag{1}$$

time-averaging over the electric field oscillations, the Stokes parameters of this field are defined as:

$$I \equiv \langle E_x^2\rangle + \langle E_y^2\rangle, \tag{2}$$
$$Q \equiv \langle E_x^2\rangle - \langle E_y^2\rangle, \tag{3}$$
$$U \equiv \langle 2E_xE_y\cos(\phi_x-\phi_y)\rangle, \tag{4}$$
$$V \equiv \langle 2E_xE_y\sin(\phi_x-\phi_y)\rangle, \tag{5}$$

where I is the intensity, Q and U describe the linear polarization, and V quantifies the circular polarization of the electric field. The CMB is linearly polarized so $V = 0$. If the source is a black body radiator in the Rayleigh-Jeans portion of the spectrum, then the observed Stokes parameters are $I \propto (T_x + T_y), Q \propto (T_x - T_y)$ with the proportionality constants fixed by calibrating the receiver system.

The signal produced by differencing the two linear polarization-sensitive bolometers when the microwave signal is Faraday modulated is

$$V_{diff} = S \times \eta_{opt}\eta_{pol}[Q\cos 2\theta(t) + U\sin 2\theta(t)] \tag{6}$$

where the (time dependent) modulation angle is

$$\theta(t) = B_z(t)\gamma l\sqrt{\epsilon}/2c, \tag{7}$$

and l, ϵ, γ, and S are the ferrite's length, dielectric constant ($\simeq 12$), gyromagnetic ratio of the electron, and the bolometric sensitivity in V/W, respectively. $B_z(t) = H_z^{app}(t) + 4\pi M_z(t)$ is the (time-dependent) magnetic induction.

3.3. Performance

In order to be useful as a linear polarization modulator the FRM must rotate mm-wave radiation with high modulation efficiency, low loss, and little degradation of polarimetric fidelity. We divide the performance criteria into four classes (electromagnetic, thermal, modulation, polarization systematics). When multiple devices are used, as with BICEP, we must ensure that the devices are matched in performance and have reasonable operating requirements. To determine if the FRMs could achieve these goals, extensive testing on individual devices (as in Fig. 5) at room temperature, and on arrays of FRMs at cryogenic temperatures (4.2 K) were performed.

3.3.1. High-Frequency Electromagnetic Performance Faraday rotation modulator was constructed for use with polarization sensitive bolometers over the frequency range 80 to 110 GHz. Figure 6) shows the insertion and reflection loss of the rotator versus frequency measured at room temperature on a vector network analyzer (VNA). Rectangular-to-circular transitions were used to couple power from the VNA to the waveguide ports of the FRM. Excellent agreement was found between its measured and performance simulated using Ansoft's High Frequency Structure Simulator. The average microwave transmission efficiency of the rotator is 80% and the band-averaged reflection loss is less than 1% across a 27 GHz band (28% fractional bandwidth). Similar devices operating from 130-215 GHz have been produced, and 49 devices operating in the 100 and 150 GHz bands have been cooled to 4.2 K and used as polarization modulators.

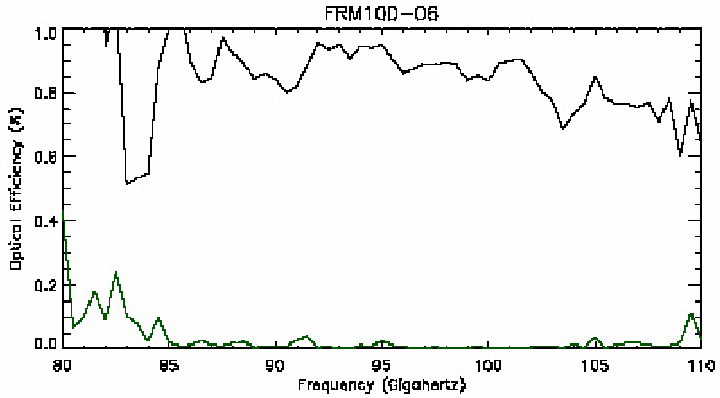

Figure 6. Optical efficiency (transmission) measurements of a 100 GHz Faraday rotation modulator at 300 K measured on a vector network analyzer. The band-averaged transmission for the modulator is 80% warm, and improves to approximately 85% when cooled below 10 K. The reflection (black) and absorption (green line) features at 83 GHz are arbitrary and determined by the desired high-pass cutoff frequency of the corrugated waveguide.

3.3.2. Polarization Modulation Performance To determine the Faraday rotator's suitability for use as a polarization modulator, a 80-100 GHz bolometric test receiver was constructed. The receiver consists of a corrugated feedhorn, Faraday modulator and polarization sensitive bolometers operating at 0.3 K, as shown in Fig. 8. The bolometers were calibrated using unpolarized thermal loads and the receiver was configured to view a 100% polarized source produced by a wire grid polarizer and a 300 K load reflected from the grid and 77 K transmitted through the grid. This source presents a 100% polarized signal with an antenna temperature of 223 K into the receiver which was subsequently modulated by the Faraday rotator.

- **Rotation Angle**
  The Faraday rotator's polarization rotation angle was determined using a polarizing grid. The FRMs were confirmed to continuously rotate polarized millimeter wave radiation by as much as 160°.
  To determine the rotation angle, the maximum and minimum detector output voltages were determined. Since the PSBs are absorbing polarization analyzers, a maximum voltage is produced when the wire-grid axis is oriented perpendicular to the bolometer's sensitivity axis. The bolometer's voltage is minimized when the grid azimuthal angle is rotated by 90° from the maximum. If the grid is positioned midway between the two bolometers, then the polarization rotation angle is given in terms of the bolometer output voltage by:

$$\Theta = \frac{1}{2}\arcsin\Big(\frac{V-(V_{max}+V_{min})/2}{(V_{max}-V_{min})/2}\Big), \tag{8}$$

  where V_{max}, V_{min} are the maximum and minimum signal voltages recorded during complete polarization modulation.
- **Modulation Modes: Continuous Polarization Angle Rotation vs. Switched/Stepped Rotation**
  From equations 3 and 4 we see that when the electric field produced by the grid is at 45° to each bolometer, $Q = 0$ and U is maximized. If the Faraday modulator is then driven into saturation to rotate the incident polarization angle by +45°, the Stokes parameters (in antenna temperature units) will be $Q = 223K$ and $U = 0K$.
  If the current is sinusoidally varied up to the current required for magnetic saturation: $I = I_{sat}\sin\omega t$, the rotation angle will be $\theta(t) = \Theta_o \sin\omega t$ where $\Theta_o = M_{sat}\gamma l\sqrt{\epsilon}/2c$ is in radians, and the difference between the (orthogonally polarized) bolometer signals $V_{x,y}$ is:

$$\begin{aligned}\Delta V(t) &= V_x - V_y \\ &\propto \cos^2(\frac{\pi}{4} - \Theta_o\sin\omega t) - \cos^2(\frac{\pi}{4} + \Theta_o\sin\omega t) &(9)\\ &= \sin(2\Theta_o\sin\omega t). &(10)\end{aligned}$$

  Figure 7 shows sample waveforms for three different magnetic bias values (polarization rotation angles).
  Phase sensitive demodulation of $\Delta V(t)$ at the current bias frequency, ω, produces a signal:

$$\begin{aligned}S = \int_0^\pi \Delta V(t)\sin\omega t dt &= \int_0^\pi -\sin(2\Theta_o\sin\omega t)\sin\omega t dt \\ &= gJ_1(2\Theta_o) &(11)\end{aligned}$$

  where $J_1(x)$ is the first-order Bessel function and g accounts for the gain of the lock-in (and numerical factors). As shown by Nanos [33], S is maximized when $\Theta_o = 52.7°$. Since $\Delta V(t)$ is not a pure sinusoidal signal, higher (odd) harmonics are also present, decreasing as $J_n(2\Theta_o)$. For BICEP however, we chose to modulate in a switched mode where the polarization was rotated by ±45°, having the effect of switching between the Stokes parameter $\pm Q$ in the bolometer coordinate system.
  Taking the difference of the bolometer signals is a measure of the value of the Stokes Q parameter (in the coordinate system defined by the two bolometers). As the grid rotates the difference signal varies exactly as in equation 6, with $\theta(t)$ equal to the azimuthal angle of the grid about the optical axis. This measurement describes the detection of linearly polarized radiation with 100% polarization modulation efficiency (in the sense that no other modulator can produce a larger differential signal).

3.3.3. Polarimetric Fidelity Three primary systematic effects corrupt polarimetry: instrumental polarization, cross-polarization, and depolarization. Instrumental polarization (IP) results from spurious coupling of the polarimeter (modulator, analyzer, and detectors) to unpolarized radiation. The IP for the bolometric receiver shown in Fig. 8 (with the polarizing grid removed) was determined by observing unpolarized thermal loads (either 300 K or 77 K) and measuring the bolometer difference signals produced as the Faraday modulator was square-wave biased at $\sim$ 1Hz. If there is non-zero instrumental polarization produced by either the optical system and/or the FRM , the two orthogonal bolometer signals will be 180° out of phase, and the amplitude of the bolometer signals will scale with the load temperature. The sum of optical and electrical (cross-talk) IP contributions of the polarimeter has been limited to $< 2\%$ for FRMs used in BICEP.

Instrumental polarization can arise from asymmetry in the toothpick structure. Asymmetries arise both in the construction of the toothpick and its placement in the waveguide. Both the tilt of the toothpick and its concentricity in the waveguide must be controlled to minimize spurious mode conversion from the desired HE^{11} mode to higher order modes. Mode conversion produces differential transmission of the two (degenerate) HE^{11} polarization states, resulting in IP. The alumina cones are manufactured with 0.5° tilt and the ferrite cylinder faces are parallel to better than 0.1°. The assembled toothpick is then placed concentrically in the corrugated waveguide.

When viewing unpolarized thermal loads at 300 K, 77 K, and $\sim$ 12K the IP signals can be seen in real time when the FRM is AC biased. The observed $\sim 1\%$ instrumental polarization is consistent with HFSS simulations of the FRM with a $\sim 0.5°$ tilt of the ferrite/alumina toothpick with respect to the corrugated waveguide axis. Since the level IP is constant in time and spatially fixed with respect to the feed and detectors, unlike a polarized celestial source, it can be removed with high-precision. Cross-polarization measurements are also in agreement with HFSS simulations and are consistent with non-orthogonality of the PSBs at the $< 1°$ level.

Depolarization arises due to differences in loss between the two helicity states which propagate in the ferrite. The two helicity states can be written in terms of the linear polarization states

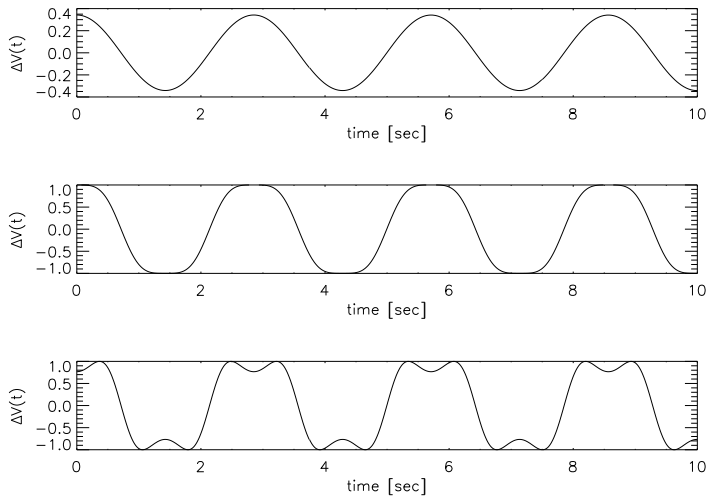

Figure 7. Simulated difference signals (Eq. 10) for orthogonally polarized bolometers viewing a polarized source whose polarization plane is rotated using a Faraday modulator. The bias modulation waveform for all curves is a 2.2 Hz sinusoid with current amplitude set to rotate linear polarization by 10° (top), 45° (middle), and 65° (bottom).

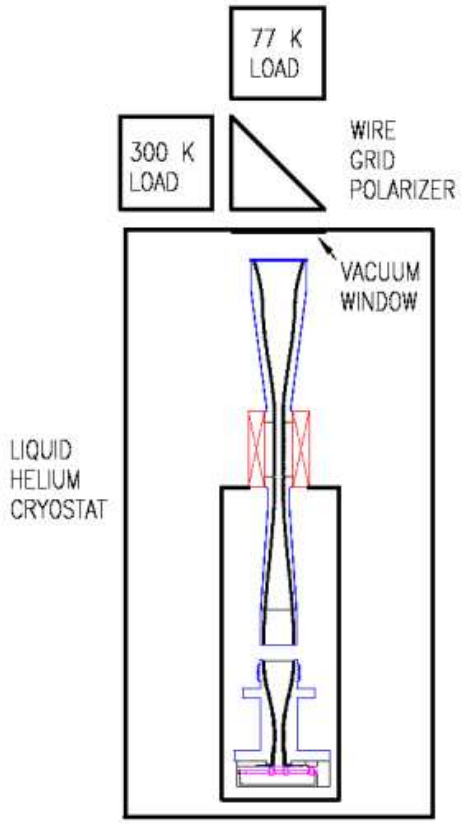

Figure 8. Test set-up for polarization modulation angle, modulation efficiency, and instrumental polarization measurements. Two polarization-sensitive bolometers view a 100% polarized thermal load produced by a wire-grid polarizer tilted at 45° with respect to the optical axis. For measurements of instrumental polarization, the grid is removed and different temperature loads are viewed.

as: RCP $= (\mathrm{E_x}\hat{\mathbf{x}} + \mathrm{iE_y}\hat{\mathbf{y}})/\sqrt{2}$ and LCP $= (\mathrm{E_x}\hat{\mathbf{x}} - \mathrm{iE_y}\hat{\mathbf{y}})/\sqrt{2}$.

At the operating frequencies of interest ($\sim$ 100 GHz) – well-above the Larmor resonance frequency of saturated TT2-111 ferrite ($\simeq$ 11 GHz) – the difference in attenuation coefficients between the two helicity states is $\alpha_+ - \alpha_- < 0.001$ Np/m. This implies that RCP electric fields are attenuated by $e^{\alpha_+} = 0.9968$ and LCP fields are attenuated by $e^{\alpha_-} = 0.9964$. This differential attenuation therefore results in *depolarization* (as opposed to *instrumental polarization*). The polarimeter's signal is the difference between the power in each polarization state, which is proportional to the difference in intensity between the orthogonal polarizations (which is also proportional to the Stokes Q parameter).
So

$$Q = |E_x^2| - |E_y^2| = 2\mathrm{LCP} \times \mathrm{RCP}$$

implying $Q_{out} = 0.993\, Q_{in}$ and $U_{out} = 0.993\, U_{in}$. This shows that the polarization angle

$$\tan^{-1} Q_{out}/U_{out} = \tan^{-1} Q_{in}/U_{in},$$

Table 1. Measured properties of 100 and 150 GHz Faraday Rotation Modulators.

Property	Value
Absolute RF Transmission (Warm)	80%
RF Reflection (Warm)	$< 3\%$
Current Required for $\pm 45^\circ$ Rotation	± 130 mA
Power Dissipation (4 K)	$\simeq 1$mW
Polarization Modulation Efficiency (4.2 K)	$\simeq 99\%$
Intrinsic Instrumental Polarization (4.2 K)	$< 2\%$
Cross-polarization (4.2 K)	$< 1\%$
Depolarization (4.2 K)	$< 1\%$

which implies that the output polarized intensity is 99.6% of the input and there is no cross polarization (spurious rotation between $E_x\hat{\mathbf{x}}$ and $E_y\hat{\mathbf{y}}$ or, therefore, between Q and U).

All three polarimetric systematics have been found to be stable over, at least, week-long time periods. This is not surprising as the three systematic effects are intrinsic to the materials used and/or caused by the construction. The stability of these offsets allows them to be modelled and subtracted from the data.

3.3.4. Magnetothermal Performance The Faraday modulator uses a superconducting solenoid that requires a magnetic bias $H_{applied} \simeq 30$ Oersted. Large variations in the magnetic field can produce eddy current heating. Careful thermal and magnetic design is therefore required to minimize eddy currents induced in the modulator. In general, eddy current heating effects are proportional to the sample area transverse to the applied magnetic field. For a solenoid made with copper magnet wire, Joule heating of the coil dominates the electromagnetic loss. Eddy current dissipation in the metallic waveguides is ten times smaller than the coil dissipation ($\sim 200\mu$W) for a solenoid that produces the ~ 30 Oersted field required to saturate a 5 Hz sinusoidally-biased ferrite. For a perfect superconducting coil, the coil loss is zero and the total modulator eddy current heating scales as the modulating frequency squared. Simulations using Ansoft's Maxwell SV are in excellent agreement with measurements of the eddy current dissipation of the Faraday modulator from DC to 20 Hz. Magnetic shielding of the bulk experimental volume/bolometers is accomplished by enclosing the solenoid in a high magnetic permeability jacket fabricated from Cryoperm 10.

3.3.5. Observations of galactic polarization using Faraday Rotation Modulators The faintness of the CMB polarization signal demands exquisite control of instrumental offsets. There are two ways to mitigate offsets: (1) minimize the offset and (2) modulate the signal before detection (Dicke switch) faster than the offset fluctuates. The BICEP experiment [21] does both. A bridge-circuit differences the two PSBs within a single feed, producing a (first) difference signal that is null for an unpolarized input. This minimizes the offset. For six of BICEP's 49 spatial pixels, the polarized signal input is rapidly modulated (second difference) by Faraday Rotation Modulators (FRM) that rotate the plane of linear polarization of the incoming radiation. The FRMs make use of the Faraday Effect in a magnetized dielectric. Polarization modulation allows the polarized component of the CMB to be varied *independently* of the temperature signal, allowing the response of the telescope to remain fixed with respect to the (cold) sky and (warm) ground. This two-level differencing scheme allows for two levels of phase-sensitive detection, allowing optical systematic effects, associated with the telescope's antenna response pattern (which could leak the much-larger CMB temperature signal to spurious CMB polarization), to be distinguished from true CMB polarization.

BICEP conducted observations of the galactic plane using FRMs during the austral winter of 2006. Several hundred hours of data were taken with the FRMs biased with a 1 Hz square wave. This modulation waveform effected $\pm 45^\circ$ of polarization angle rotation. Other modulation waveforms can provide more or less rotation, as desired. To validate the FRM technology we targeted several bright regions of the galactic plane. Results from some of these observations are displayed in Figure 9, where we also show the same region as imaged by WMAP [34].

3.4. Conclusions

The Faraday Rotation Modulator described in this white paper represents a new form of polarization modulation. Due to its wide-bandwidth performance, high modulation rate, and ability to operate at cryogenic temperatures it is uniquely capable as a polarization modulator for CMB applications. The solid-state nature of the device combined with the ability to mass-produce devices also implies it is suitable for array applications – sure to be an essential component of all future probes of the polarization of the Cosmic Microwave Background radiation.

3.5. Acknowledgments

This project has been supported by the Caltech President's Fund and by the University of California, San Diego and NSF PECASE Award # AST-0548262. Evan Bierman assisted in the design, development, and fabrication of the FRMs used in BICEP. Thomas Renbarger and Evan Bierman provided figures used in this paper. Ed Wollack and Neal Erickson provided many useful insights as well as assisting with design considerations. Helpful comments from Jamie Bock, Darren Dowell, William Jones, Chao-lin Kuo, Andrew Lange, and Ki Won Yoon are gratefully acknowledged.

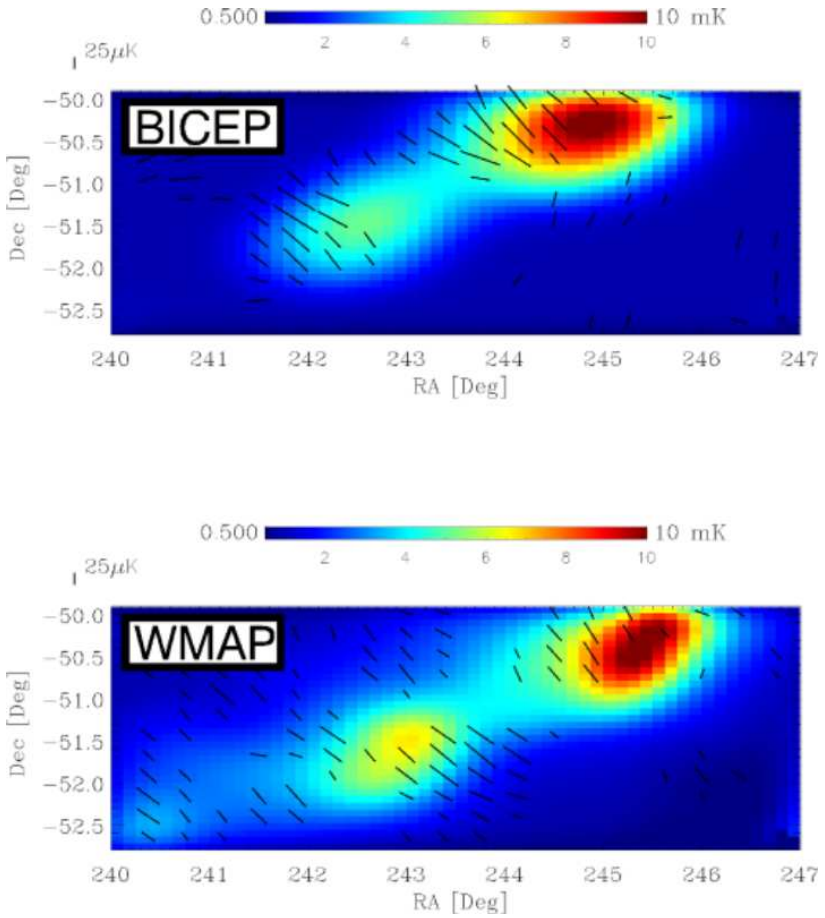

Figure 9. Map of a portion of the galactic plane made using one of BICEP's six Faraday Rotation Modulator (FRM) pixels (top) operating at 100 GHz, compared to WMAP's observations of the same region (bottom). Microwave radiation is polarized by dust grains preferentially aligned by the galaxy's magnetic field. The FRM pixels modulate only the polarized component of the emission and can fully characterize linear polarization *without* rotation of the telescope. The short lines indicate the magnitude and orientation of the plane of polarization, and the color scale indicates the temperature range. For comparison, a scale bar representing 25 μK linear polarization is shown. The galactic plane extends approximately from the lower left to the upper right of each map. Both maps show significant linear polarization orthogonal to the galactic plane[34]. Similar maps were produced for BICEP's 150 GHz FRM pixels. We note that the BICEP FRM data were acquired over the course of only a *week* of observations. Figure credit: Evan Bierman.

Journal of Physics: Conference Series **155** (2009) 012006 doi:10.1088/1742-6596/155/1/012006

4. Quasioptical Reflective Polarization Modulation for the Beyond Einstein Inflation Probe

David T Chuss

NASA Goddard Space Flight Center, Code 665, Greenbelt, MD, 20771 USA

E-mail: David.T.Chuss@nasa.gov

Abstract. Polarization modulators that are based on the introduction of a quasioptical phase delay between two orthogonal linear polarizations are reviewed. The general principle behind the device and the application to the Beyond Einstein Inflation Probe are addressed.

4.1. Introduction

Polarization modulation allows for clean separation of the polarized light from a source and the unpolarized background. This is likely to be an important element in systems designed to search for the B-mode polarization as the unpolarized contribution from the Cosmic Microwave Background (CMB) is much larger than the faint signature of inflation.

It is desirable that a polarization modulator not change the total coherence of the signal that it is modulating. That is, for polarization modulation having low systematics, it is advantageous, and perhaps required, that the total polarization ($P^2 = Q^2 + U^2 + V^2$) remain the same throughout the modulation process. This corresponds to a path on the Poincaré sphere. Such an operation can be physically produced by introducing a phase delay between two orthogonal polarization states. group SU(2) or equivalently by Mueller matrices that are members of

Though there are various ways to do this in practice, this white paper will explore techniques that do this quasioptically and in reflection by adding a phase delay between orthogonal *linear* polarizations. This is most commonly done using a system of polarizers and mirrors. Specifically, it will focus on the Variable-delay Polarization Modulator (VPM). This device modulates the phase between two orthogonal linear polarizations by changing the separation between a grid and mirror. A major advantage of this device is that it can be constructed large enough to be used as the first element in the optical system thereby avoiding most of the instrumental polarization of the system. It can also modulate polarization on time scales (∼few Hz) that will allow 1/f mitigation to be done in polarization rather than in a spatial scanning mode. This combination of front-end placement and modulation in polarization is a potential advantage of the VPM since it avoids systematics that mix unpolarized anisotropy into a false polarization signal. Calibration techniques associated with such an architecture may be especially suited to polarimetry at large angular scales where scanning calibration schemes are challenging. In addition, the symmetry of the polarization separation in the VPM can be exploited to provide additional systematic controls.

4.2. Heritage

This concept has heritage in the Martin Puplett interferometer (hereafter MPI) [35] which utilizes a variable phase introduction between two orthogonal linear polarizations to generate an interferogram that, when Fourier transformed, gives spectra of Stokes Q and V. The most common use of this device is as a spectrometer. In such an application, Stokes I of the input signal is mapped to Stokes Q using a polarizing grid (and Stokes V is set to zero) such as in the case of COBE/FIRAS [36]. Even so, the utility of an MPI as a polarization modulator was recognized in early works on the subject [37]. An MPI has been used in the MITOpol CMB

spectropolarimeter [38, 39] in combination with a rotating Fresnel double rhomb for the purpose of characterizing the polarization spectrum of the CMB.

A more compact way of introducing a phase delay between two orthogonal polarizations is by placing a polarizing grid in front of and parallel to a mirror. The phase delay is then a function of the mirror-grid separation. Various implementations of this architecture exist in the literature. Howard [40] implements such a system as a polarization transforming reflector (PTR) operating at 1.05 mm. Such setups are common in microwave and radio applications for transforming polarization states. Houde [41] models a similar device (called a "reflecting polarizer" for an OVRO receiver that is used to transform the linear polarization from dust emission into circular polarization that is cross-corellated in the receiver [42]. A similar quarter-wave transformer was also used earlier by Erickson [43] for work at 0.9 mm.

A similar grid-mirror system has been employed by Manabe[44]. In this work, two such systems (here dubbed a "frequency-selective polarizer" or FSP) are used as an alternative to an MPI for interferometry. These authors find that such a system has more alignment tolerance than the MPI, but also introduces an added complexity of treating resonances in the grid-mirror cavity.

Erickson[45] has used a variant called a "Reflecting Polarizing Interferometer" (RPI) in which the grid-mirror cavity is filled with a dielectric. In this work, the RPI is tested as a filter element as an alternative to a Fabry-Perot interferometer.

Polarization modulation with grid-mirror devices has also been done. For such applications, it is possible to modulate polarization in one of two ways. First, one can vary the grid-mirror separation such as is done in the interferometric applications. Second, it is possible to use the device as a half- or quarter- wave plate by fixing the grid-mirror separation (usually to $\lambda/2$ or $\lambda/4$) and rotating the device. The former has been demonstrated in the submillimeter by Krejny[46] in which two VPMs are used to navigate the Poincaré sphere [47]. The Cosmic Foreground Explorer (COFE) used this type of modulation in an early configuration [48], but later moved to a spinning reflective-half wave plate (HWP) modulation [49]. Shinnaga[50] and Siringo[51] have also used the spinning reflective half-wave plate in the submillimeter.

The remainder of this white paper will focus on polarization modulation devices using the parallel grid-mirror system.

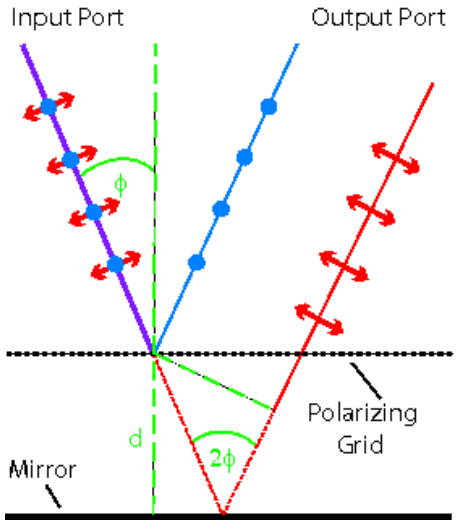

Figure 10. A phase delay between two orthogonal linear polarizations is introduced by an architecture in which a polarizing grid and a mirror are placed parallel to one another. The dotted red line indicates the physical path difference between the two polarizations.

4.3. Operational Principle

The basic architecture that all of the grid-mirror systems discussed in the Introduction is shown in Figure 10. Radiation of an arbitrary polarization state is incident on the grid-mirror structure. The component of the light that is linearly polarized parallel to the grid wires reflects off of the grid. The orthogonal component gets transmitted by the grid, is reflected by the mirror and then passes through the grid again. The two beams recombine with a phase that is related to the path length. The path length is in turn a function of the incident angle and the grid-mirror separation.

$$l = 2d\cos\phi \tag{12}$$

This path difference gives a geometric phase delay of

$$\Delta = \frac{2\pi l}{\lambda} = \frac{4\pi d\cos\phi}{\lambda} \tag{13}$$

Assuming that the wires are perfect polarizers and the grid wires are oriented at an angle θ with respect to the coordinate system of interest, the Mueller matrix for this system is

$$\begin{pmatrix} 1 & 0 & 0 & 0 \\ 0 & \cos^2 2\theta + \cos\Delta \sin^2 2\theta & -\sin 2\theta \cos 2\theta(1-\cos\Delta) & \sin 2\theta \sin\Delta \\ 0 & \sin 2\theta \cos 2\theta(1-\cos\Delta) & -\sin^2 2\theta - \cos\Delta \cos^2 2\theta & -\cos 2\theta \sin\Delta \\ 0 & \sin 2\theta \sin\Delta & \cos 2\theta \sin\Delta & -\cos\Delta \end{pmatrix} \tag{14}$$

For the case of the VPM, the angle is held fixed and the phase is modulated. Setting $\theta = 45^\circ$ gives

$$\begin{pmatrix} 1 & 0 & 0 & 0 \\ 0 & \cos\Delta & 0 & \sin\Delta \\ 0 & 0 & -1 & 0 \\ 0 & \sin\Delta & 0 & -\cos\Delta \end{pmatrix}. \tag{15}$$

This operation is a combination of an inversion operation and rotation about the U-axis on the Poincaré sphere. Because of this, Stokes U is unmodulated, so full linear polarization measurement requires an additional step. Since Δ is dependent on wavelength, the modulation will become less coherent at higher orders, forming an interferogram that contains information about the polarization spectrum of the source.

Conversely, for the reflective HWP, $\Delta = \pi$ and is fixed. The general matrix reduces to

$$\begin{pmatrix} 1 & 0 & 0 & 0 \\ 0 & \cos 4\theta & -\sin 4\theta & 0 \\ 0 & \sin 4\theta & \cos 4\theta & 0 \\ 0 & 0 & 0 & 1 \end{pmatrix} \tag{16}$$

which is recognizable as the Mueller matrix representing a HWP. Note that the path on the Poincaré sphere in this case is a circle in the Q-U plane. Here, linear polarization is completely modulated. Bandwidth effects dilute the signal in a direction perpendicular to the path in the Q-U plane, so the efficiency of the ideal reflective HWP is constant over the modulation, but falls off with increasing bandwidth. This architecture is tunable to multiple bands by changing the grid-mirror separation.

4.4. Current State-of-the-Art

Krejny [46] has reported astronomical use of a dual VPM system at 350 μm. For these observations, the VPM settings were not optimized, resulting in poor modulation efficiency. Nonetheless, an instrumental polarization of less than 1% was measured. Laboratory tests of a

single VPM in this system are shown in Figure 11. In this figure, the data points represent the modulated signal as the grid-mirror separation was varied. The curve represents the polarization transfer function anticipated given the geometrical phase lag (Equation 13.) This has been adjusted in phase and amplitude to match the first peak for illustrative purposes. The difference in the observed phase as compared with that anticipated from the geometrical relationship is most likely due to the fact that the grid wires in this system are a measurable fraction of the wavelength (25 μm vs. 350 μm). This results in a phase shift contribution that is due the reactance of the system. This issue can be resolved by working in a regime where the wires are much smaller than the wavelength. The same VPM has been measured in a 3.15 mm system [52] and this effect was not observed (see the right side of Figure 11). In this plot, the solid line is the polarization transfer function based on the geometric phase delay between the two polarizations.

The polarization modulation efficiency is ∼80% for the 350 μm case, but is significantly higher at longer wavelengths. Part of this difference is due to the non-ideal efficiency of the VPM grid at 350 μm. The remainder is most likely due to differences in the optical systems in the two measurements.

This phase-separation relationship needs to be further quantified, especially in the application of VPMs to spectropolarimetry. The wire size, or perhaps more generally the set of polarizer parameters, is a key design consideration in constructing and implementing VPMs.

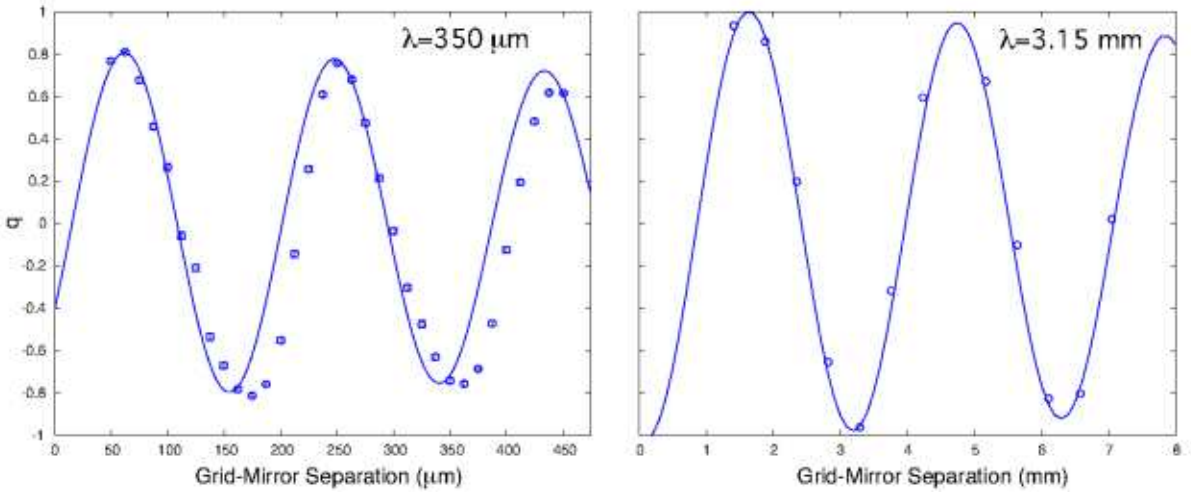

Figure 11. (left) The Hertz/VPM (350 μm) laboratory data is shown [46]. The solid line represents the model for a geometric phase delay that is phase and amplitude matched to the first peak of the data. (right) The same VPM was also tested at 3.15 mm. In this case, no phase or amplitude adjustment was done; the phase more closely matches that of the geometrical case. In each case, the bandwidth is ∼10%

4.5. VPMs and CMB Polarization

The systematics of a VPM systematics as they apply to CMB polarimetry are highly-coupled to the instrument architecture in which the VPM is employed, so such a concept is briefly described here. We note as an aside that this differs from the Hertz/VPM implementation mentioned in the preceding section.

Figure 12 shows an optics concept for which the VPM is suited. In this case, the symmetry of the VPM is utilized. The VPM is the first element in the optical path in order to minimize

instrumental polarization. This concept requires an array of polarized detectors with the direction of polarization sensitivity oriented at a 45° angle with respect to the wires of the VPM. For the ideal case, this system is described by expression 15. To first order, this system is insensitive to Stokes U, and thus requires an additional parameter (such as spacecraft or instrument rotation) to fully map the linear polarization. However, to counter this disadvantage, this system allows many of the systematic effects to be hidden in Stokes U without affecting the measurements of Stokes Q.

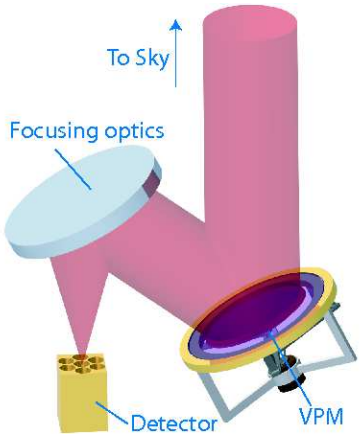

Figure 12. The optical path includes a VPM as the first component in the system.

4.6. Systematic Effects
In many ways, the advantages and disadvantages of reflective HWP are similar to dielectric HWPs, so the following discussion of systematics will focus on the VPM configuration. However, where appropriate below, work on reflective HWPs will be included since it gives valuable insight into the electromagnetics of the grid-mirror system.

4.6.1. Beam Walkoff For the mirror-grid system, the two polarizations are displaced relative to one another a distance $x = 2d \sin \phi$. This quantity, x, is the "walkoff" and for the VPM varies with the modulation variable, d. This leads to a potential synchronous pickup; however this can be mitigated in two ways. First, this effect can be reduced by choosing small incidence angles. Second, if the VPM is located at a pupil in the optical system, then a parallel shifting of the output beams will not change the relative angle between the beams in the two orthogonal polarizations.

4.6.2. Variable Beam Truncation At non-normal incidence, the back optical surface of the VPM will be vignetted by the frame of the front optical surface. The amount of vignetting will depend on grid-mirror separation and so will vary with the modulation. An adequate edge taper will ameliorate this problem. In addition, the symmetry of the concept can help as well. The beam truncation is such that it will affect the Stokes U polarization state. Variations in the light reflected off of the back surface of the VPM will show up in each of the (polarized) detectors as common-mode variations and can be differentiated from the antisymmetric variation of the modulated Q polarization state. Of course, this is only strictly true for the central ray of the system and the effect of beam truncation will vary across the array.

4.6.3. Grid Emissivity and Resonances from Trapped Modes. The emissivity of the grid wires will combine with polarization leakage to cause emission and absorption that will be a function of the grid-mirror separation. Cooling the VPM to 2.73 K will mitigate this risk, but this will impact spacecraft design and will certainly require development effort for cryogenic VPMs. Again, the symmetry of the system helps here as well. Emission and absorption will affect the Stokes U value, but will appear as common-mode in the two orthogonal detectors. The full effect of this will need to be studied in more detail.

An additional effect of imperfect polarization isolation is that radiation can become trapped between the grid and the mirror. This effect has been observed in such grid-mirror systems (for an example, see Houde[41]). This effect is also thought to be responsible for the complex interferometer behavior in Manabe[44]. For broadband operation, this effect is diluted significantly. In addition, optimizing the wire size for the wavelength range will also help mitigate this problem.

4.6.4. Dependence on Grid Properties Extensive literature has been devoted to the electromagnetic modeling of polarizing grids (see Houde [41] and references therein). In the limit where the wavelength is much larger than the wire diameter, the polarizing grid approaches ideal behavior with high isolation between the two orthogonal polarizations. In this case, the phase delay introduced by a VPM is proportional to the path difference between the two polarizations as stated above. As this assumption is violated, the phase delay acquires a contribution due to a reactive component that has a nontrivial dependence on grid-mirror separation. This has been noted by Krejny[46]; however the effect requires more study.

4.7. Technology Development

4.7.1. Parallel Transport Mechanism In order to ensure that the two beams recombine at the same angle, and that the phase difference is well-defined, it is essential that the transport mechanism used to control this mechanism maintain parallelism. This problem is similar to that encountered in Fabry-Perot systems, and similar tolerances apply. One way of constraining parallelism is to employ a system of 3 motors with feedback to control the parallelism [53]. Another is to mechanically constrain all but one degree of freedom and control the position with a single feedback loop [54]. The latter has been implemented in the Hertz/VPM submillimeter polarimeter [55].

The Hertz/VPM devices used piezoelectric motors for motion. The COFE modulator used a linear coil-based motor. In the latter case, the transport stage was driven at resonance to ease control for fast modulation. The feedback can be controlled with a variety of sensors including capacitive devices as well as optical encoders.

4.7.2. Grid Construction In order to implement modulation at the primary aperture for Inflation Probe, VPMs will have to exceed 50 cm in diameter. Grids are typically made by wrapping wire over the grid frame [56]. An alternative technique is based on work by Novak[57] and involves wrapping wires onto a cylindrical mandrel and then transferring them to a grid frame. The latter technique has been used to construct a 50 cm diameter polarizing grid with 63.5 μm wires on a 200 μm pitch (See Fig. 13). The resonant frequency of the wires was greater than 128 Hz, much larger than the $\sim$few Hz modulation frequency. Using the grid flattener, a planarity of the grid surface that was below 50 μm was achieved.

Because the phase definition is of utmost importance with a VPM, the wire surface must be flat to a small fraction of a wavelength. Grid flatteners have been used in both the Hertz/VPM VPMs [55] and in the prototype CMB wire grid [58].

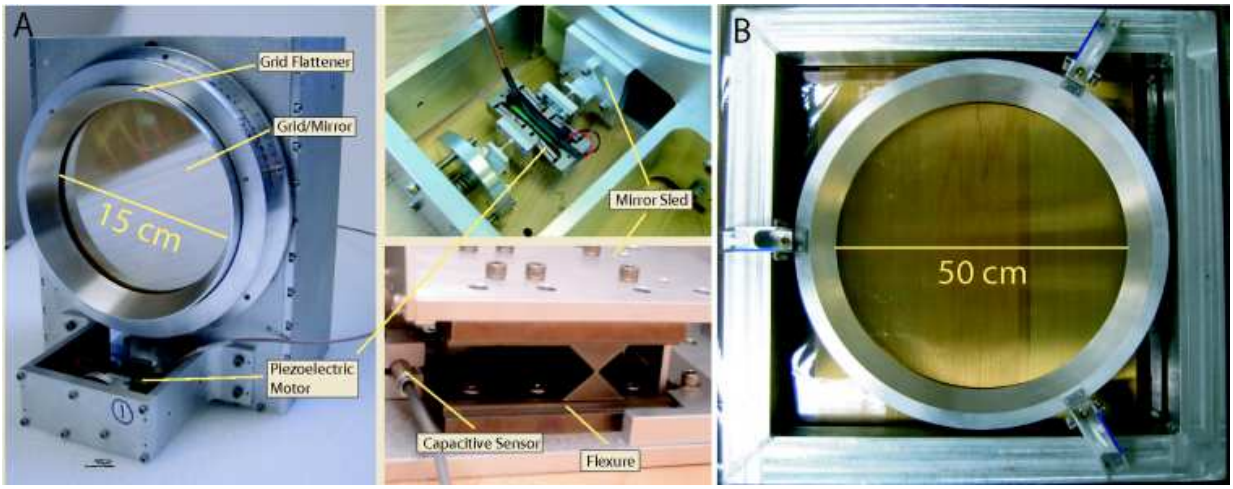

Figure 13. The VPM used in the Hertz/VPM experiment is shown in (A). A 50 cm diameter grid with grid flattener is shown.

4.8. Summary of VPM Advantages/Disadvantages

Advantages

- VPMs are a practical solution for modulation at the front of the optical system because they can be made larger than dielectric HWPs and operate in translation rather than rotation.
- The interferometric modulation scheme provides potential for multi-band, broad-band, or spectropolarimetric use.
- Primary modulation can be done in polarization rather than photometric scanning.
- The translational flexure is frictionless and can be engineered for long, reliable operation in space.
- Systematic control has the potential to be high, due to the capability of "hiding" systematics (e.g. those due to differential loss) in the unmeasured linear Stokes parameter.
- The sensitivity to Stokes V can provide an additional calibration tool.
- "Leakage" term is V rather than U, and therefore VPM may provide good control of (E, B) mixing systematic.
- No transmissive dielectrics are required, thereby mitigating dielectric loss, cavity formation, and large cosmic ray cross section.

Disadvantages

- The VPM is not as tested as the HWP (VPM is at TRL 3).
- Measurement of only one linear Stokes parameter at a time requires spacecraft rotation or cross-calibration with another optical system for complete polarization determination.
- The use of VPMs for front-end modulation would be problematic for high angular resolution experiments. It would be practically limited to lower multipole, large scale B-mode searches.
- Since only one linear Stokes parameter is measured at a time, the modulation efficiency for linear polarization is dependent upon the form of the modulation function. This introduces a potential integration time penalty.
- The VPM is most likely limited to systems with low enough 1/f such that the practical modulation frequencies of ∼1-10 Hz would be useful. (This would include bolometer-based systems, but perhaps not many coherent detectors).

4.9. Path to TRL 5

- The flexure concept needs to be adapted for the large aperture VPM. (1.5 Person Years + 50k)
- The continuous ∼few Hz modulation/demodulation functionality needs to be tested (1.5 Person Years + 50k)
- The flexure and grid need to be adapted for cryogenic use. (1.5 Person Years + 150k)
- Cryogenic microwave testing must be done. (1.0 Person Years + 100k)
- A system demonstration leading to astrophysical data product on ground-based or suborbital platform must be done.

5. A Metal Mesh Achromatic Half Wave Plate

G Pisano[1], G Savini[2], P A R Ade[2], and V Haynes[1]

[1] The University of Manchester, School of Physics and Astronomy - Alan Turing Building, Upper Brooke street, Manchester, M13 4PL, UK
[2] Cardiff University, School of Physics and Astronomy, Queens Buildings, The Parade, Cardiff, CF24 3AA, UK

E-mail: giampaolo.pisano@manchester.ac.uk

Abstract.
Achromatic Half-Wave Plates can be realised using photolithographic techniques. Prototypes working at 150GHz have been designed, manufactured and tested and preliminary performance results are presented [59]. This type of device could replace the usual birefringent HWP used in mm/submm polarimetry experiments.

5.1. Introduction

Birefringent material-based HWPs are used in many present experiments dedicated to the detection of the polarization of the Cosmic Microwave Background radiation. Accurate models [60, 61] have been developed which enable accurate prediction of the HWP performance and enable through design modifications a minimization of systematic effects such as instrumental and cross polarization. However, the demanding requirements for the next generation of CMB instruments, which aim to detect the very low level B-Mode signature, necessitates a new HWP concept which can be utilized with the very large arrays needed to achieve a meaningful sensitivity limit. The costs and the availability of birefringent materials of increasing size is a known problem (crystalline quartz available in $\sim$110 mm diameter boules and crystalline sapphire available in $\sim$280 mm diameter boules) so alternative solutions must be sought. The type of HWP proposed here has a very good chance of replacing the crystalline technology with one constructed from metal mesh components. The manufacture of metal mesh components is a well established technology and will not be discussed in detail here (see filter review of these proceedings).

5.2. Concept

A Half Wave Plate introduces a phase shift of 180 degrees between two monochromatic electromagnetic waves that have orthogonal polarizations and that are traveling through it. In an Achromatic HWP, this phase shift is maintained over a broader electromagnetic frequency band. When rotating, a HWP rotates any polarized incident vector at twice the angular velocity of the plate. Thus any linearly polarized incident radiation can be modulated and detected by using detectors sensitive to the polarization (analyzers, OMTs, etc.) after the HWP. The phase shift between the orthogonal axes is normally achieved using the difference between the refractive indices of the ordinary and the extraordinary axes of a birefringent material. Hence , the plate thickness determines the frequency (or multiples of it) at which the crystalline plate acts as a HWP and inherently it is only effective over a narrow frequency band. Since bolometric systems need broad photometric bands to achieve good sensitivity a single crystalline plate would prove very inefficient. A known solution to this was given by Pancharatnam [62], who demonstrated that a broader operational band can be achieved by stacking three or five plates together with appropriate rotation between their optical axes.

Here we propose an alternative solution that consists in using well know metal mesh technology to design and build submillimeter/millimeter HWP. Metal mesh grids with sub-

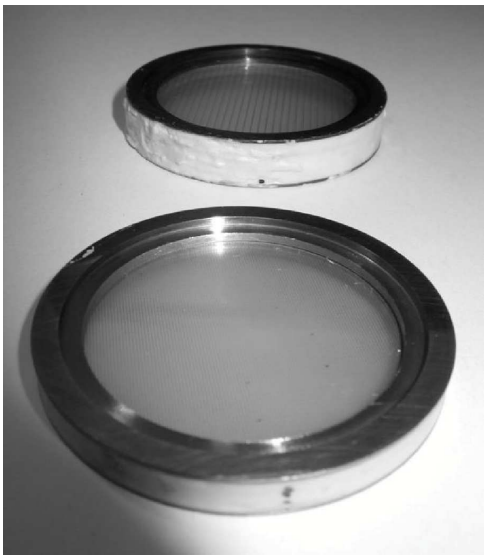

Figure 14. Pictures of the two stacks of inductive and capacitive grids of a 150 GHz Mesh-HWP. The prototype had an internal diameter of ∼35 mm.

wavelength geometries can be designed to manufacture filters for the FIR to submillimeter region. Here, the idea is to extend these studies and design grids which behave differently for orthogonal polarised input and thus to artificially reproduce the behaviour of a birefringent material. Devices of this kind have been realized in the past using other technologies to make microwave retarders at low frequencies [63]. Here we have adopted a particular geometry used in these earlier designs to construct a device able to provide a phase-shift of 180 degrees over a 40% bandwidth around the central frequency of 150 GHz. The concept of a HWP is readily visualized in metal mesh structures as the capacitive and inductive geometries [64] invoke opposite frequency dependent phase shifts. The mesh equivalent of the achromatic HWP thus requires special geometry meshes with delay lines to create a relatively flat phase of 180 degrees over the photometric bands with good in-band transmission of orthogonal polarized vectors. We have used finite-element electromagnetic analysis (HFSS) together with our own transmission line model to optimise the mesh geometries and the design of our prototype achromatic HWP. Here we describe the manufacture of a prototype device for use at frequencies near 150 GHz and compare its measured performance against the model expectations.

5.3. The 150 GHz prototype

The mesh HWP prototype is constructed from twelve meshes whose geometry was determined from the modelling. The device consists of two stacks of grids: one capacitive and the other inductive. The two stacks are built separately and mounted orthogonal to each other so that the axis of one stack is rotated with respect to that of the other stack. Each stack acts on one of the two polarization directions leaving the transmission of the other one almost unperturbed. In addition to the phase effect, the capacitive stack behaves like a low-pass filter and the inductive one as a high-pass filter. There is a spectral region where both the filters have high transmission and their individual phase shifts have opposite signs. The combined difference between phase shifts gives the required 180 degrees delay. Pictures of the capacitive and inductive stacks are shown in Fig.1.

As for many other devices used for the detection of the CMB polarization, one of the most important requirements of the HWP is to have a very low cross polarization. The expected

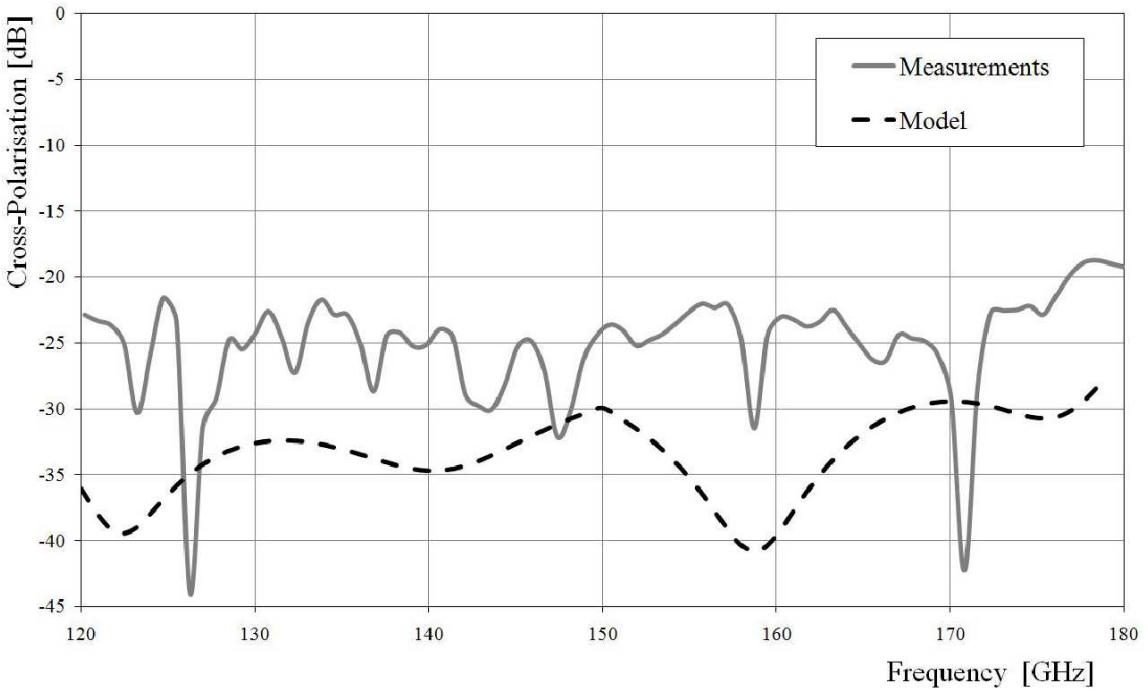

Figure 15. Predicted and measured cross-polarization performance of a 150 GHz Mesh-HWP prototype.

cross polarization for the current device is at the -35 dB level as predicted from the modelling. Measurements of the first prototype are shown in Fig.2 where the cross-polar response is observed to be about -25 dB. The measurements were made using the same experimental setup adopted in [60]. The mesh HWP was held in a rotary stage between two aligned polarizers. Initially, one of the two axes of the HWP was aligned with the polarizers using a laser. The HWP was then rotated by 45 degrees to reach a minimum corresponding to the cross-polarization signal. The discrepancy between model and data can be explained if the alignment between the grids during the assembly of the device was not perfect. However, the measured cross polarization is already comparable to that measured for crystalline devices (for multiplate HWPs we mean the mimimum achievable signal integrated over the band obtained using the same experimental setup). The modulation efficiency of this prototype is greater than 99%.

5.4. Discussion

Mesh filter modelling and its manufacture technology are well understood and filter components made in this way are considered to be mature in terms of flight readiness from usage in a number of missions (ISOLWS, Spitzer, Mars missions, Herschel, Planck). The extension to 'anisotropic' grids to manufacture a HWP has been proved to work well. The designs are scalable to any frequency in the FIR to millimeter region. Conversely, there is not a wide range of birefringent materials available. Moreover, the dimensions of commercially available crystals are limited to ; $\leq$ 28 cm diameter (sapphire only) and even then a complicated manufacture and anti-reflection coating for the three or five bonded plates need to be achieved for acceptable broadband performance. On the other hand the mesh HWP design presented here is an air-gap filter type device. It relies on very thin (1.5 μm thick) copper coated mylar substrates on which the metal mesh geometries have been produced photolithographically. The grids are kept at specific distances by means of annular metallic spacers as used in the air-gap filters used

in the cited space borne instruments. However, mesh filters can be also designed without air gaps being completely embedded into dielectric materials. These devices know as 'hot pressed' filters are very robust and like their air-gap counterparts can be cooled cryogenically. We are currently designing a modified 'hot pressed' version of the HWP presented here. Another crucial difference between the technologies is the requirement to cool the devices. For the crystalline devices cooling is essential to remove absorption from phonon bands within the material and hence eliminate emission which could prove a serious sensitivity limitation in terms of the photon noise seen by the detectors. Metal mesh will have minimal absorption throughout the FIR to millimeter region as indeed the filter technology has demonstrated and thus offers the possibility of using the devices warm facilitating simpler rotation mechanism requirements. From the systematics point of view one important aspect to be investigated is the effect of the mesh HWP on the optical beam. The effects due to normal mesh filters are known to be very low. Measurement of the mesh HWP cross polar beams are already planned.

5.5. TRL analysis

The device presented here was built using the air-gap mesh filters technology. The TRL of the present tested device is therefore rated as that of the air-gap filters (see Filter section in these proceedings). Having proved the concept, the next prototypes of mesh HWPs will be made using 'hot pressed' recipes that we have in hand. The hot pressed mesh filter technology is also space qualified. Interestingly, the next devices will therefore only differ in the mesh geometries adopted and should otherwise be considered as a mature space-qualified technology.

6. Polarization Modulation with Photolithographic Modulators

A Kogut
Code 665 Goddard Space Flight Center, Greenbelt, MD 20771
E-mail: Alan.J.Kogut@nasa.gov

Abstract. I briefly review the current status for MEMS and SIS switches for CMB polarization modulation. Photolithographic modulators allow development of a "polarimeter on a chip" capable of measuring the Stokes I, Q, and U parameters within a single beam spot on the sky but with no macroscopic moving parts. The modulators place no constraints on the optical design, while the fast switching speed (in excess of 1 kHz) relaxes constraints on beam motion across the sky. However, while some prototype switches have been demonstrated, the devices remain at low TRL.

6.1. Introduction

Reliable characterization of faint polarization superposed on a bright unpolarized foreground requires modulating the polarized signal on time scales short compared to instrumental drifts or $1/f$ noise. Of the various technologies studied in this workshop, microcircuit modulators offer the fastest modulation.

Figure 16 illustrates the concept for phase-sensitive microcircuit modulation. A polarizing microstrip element (e.g., orthogonal probes in a resonant structure) launches voltages into two arms of the polarimeter, proportional to the electric field amplitudes $E_x \cos(kz - \omega t - \phi_x)$ and $E_y \cos(kz - \omega t - \phi_y)$. A half-wave phase switch alternately injects a phase delay 0 or π in one arm. The voltages from the two arms are then combined before square-law detection. When the phase switch is off, the voltages in the two arms are

$$\begin{aligned} V_x &= E \cos\alpha \cos(\omega t - \phi_x) \\ V_y &= E \sin\alpha \cos(\omega t - \phi_y) \end{aligned} \tag{17}$$

where $E = \sqrt{(E_x^2 + E_y^2)}$ and α is the angle between the linearly polarized incident field and the xy coordinate system of the polarimeter. The detector power is

$$\begin{aligned} P_{\rm off} &= \langle (V_x + V_y)^2 \rangle \\ &= E^2(1 + 2\cos\alpha \sin\alpha) \end{aligned} \tag{18}$$

up to an uninteresting constant phase. When the phase switch is on, it introduces an additional half-wave path length so that $V_y = E \sin\alpha \cos(\omega t - \phi_y + \pi) = -E \sin\alpha \cos(\omega t - \phi_y)$. The detector power is then

$$P_{\rm on} = E^2(1 - 2\cos\alpha \sin\alpha) \tag{19}$$

As the switch chops, the detector produces a slowly-varying offset

$$\begin{aligned} P_{dc} &= (P_{\rm on} + P_{\rm off})/2 \\ &= E^2 \ \ (i.e.\ \text{Stokes I}) \end{aligned} \tag{20}$$

proportional to the unpolarized intensity, plus a rapidly modulated term

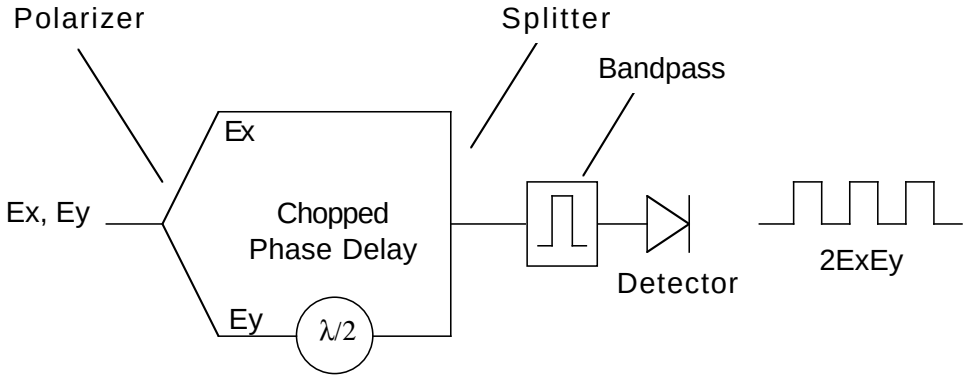

Figure 16. Schematic microcircuit polarimeter. A phase switch introduces a half-wave delay in one arm before the signals are combined and detected. The detector output has a dc term proportional to the unpolarized intensity (Stokes I) plus an ac term at the switch frequency proportional to the linear polarization. In practice, the circuit would be symmetrized with a 90° switch in each arm.

$$\begin{aligned} P_{ac} &= (P_{\rm on} - P_{\rm off})/2 \\ &= 2E^2 \cos\alpha \sin\alpha \\ &= 2E_x E_y \ \ (i.e.\ \text{Stokes U}) \end{aligned} \tag{21}$$

proportional to the linear polarization (Stokes U). We thus unambiguously separate the polarized and unpolarized components in a single measurement with a single detector.

The concept can readily be extended to provide simultaneous measurements of the Stokes I, Q, and U parameters. Figure 17 shows one such design. A polarizing element again launches voltages onto microstrip components proportional to the x and y components of the incident electric field. Each component is then split to separate detection chains. Detector A (top) is

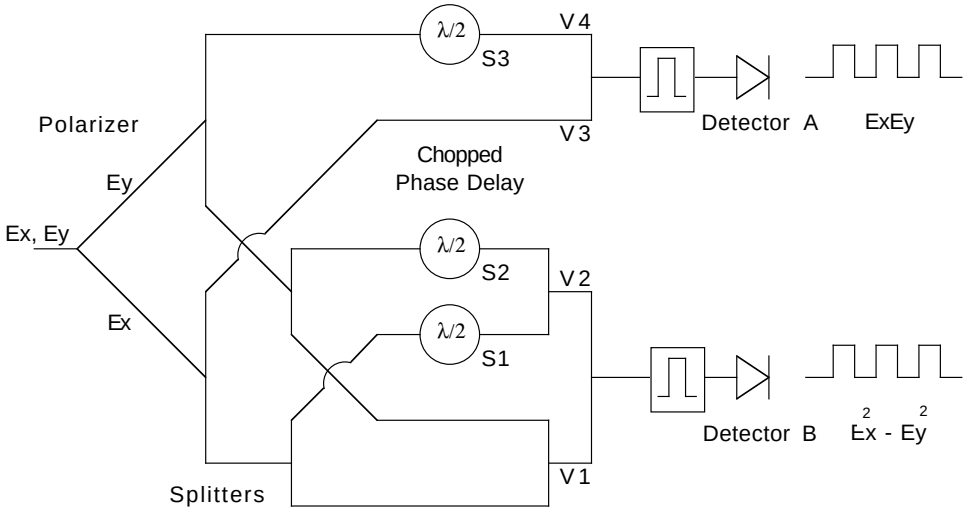

Figure 17. Schematic planar polarimeter to measure Stokes IQU components. Detector A measures the Stokes U parameter as in Figure 16. Switches S1 and S2 inject a half-wave delay out of phase with each other to allow Detector B to measures Stokes Q.

identical to the IU polarimeter in Figure 16. Detector B has an additional pair of phase switches run out of phase with each other (e.g., S1 has phase delay 0 when S2 has delay $\lambda/2$, or else S1 has phase delay $\lambda/2$ when S2 has delay 0). As switches S1 and S2 chop, detector B has a dc term proportional to Stokes I, and a modulated term $P_{ac} = E_x^2 - E_y^2$ proportional to the Stokes Q parameter. Other designs are possible. By simultaneously measuring I, Q, and U, the phase-switched polarimeter fully characterizes the incident linear polarization. This decoupling of the polarization measurement from the instrument orientation or beam scan motion greatly reduces the problem of aliasing unpolarized anisotropy into a spurious polarization signal.

To reduce systematic effects, the modulator circuit should be symmetrized so that all paths from the input to the detector encounter similar switching circuits. Figure 18 shows a symmetrized version of an IQU polarimeter. The upper circuit is configured to detect Stokes U, while the lower circuit detects Stokes Q. Each transmission line has one switch to minimize differential loss between the orthomode transducer and the detector.

6.2. Modulator Circuit

The microcircuit polarimeters described above require phase modulation in individual arms of the circuit. Delay lines of different path length provide a simple, convenient way to produce the phase shift. The simplest such circuit would synchronously switch the transmission path between two legs differing by a fixed length, which in turn would create a phase difference in the transmitted signal. The phase difference, however, would depend on wavelength so that the resulting device would operate as intended only over a narrow wavelength band. Overcoming photon noise statistics requires broad-band operation and thus more complicated circuits are required.

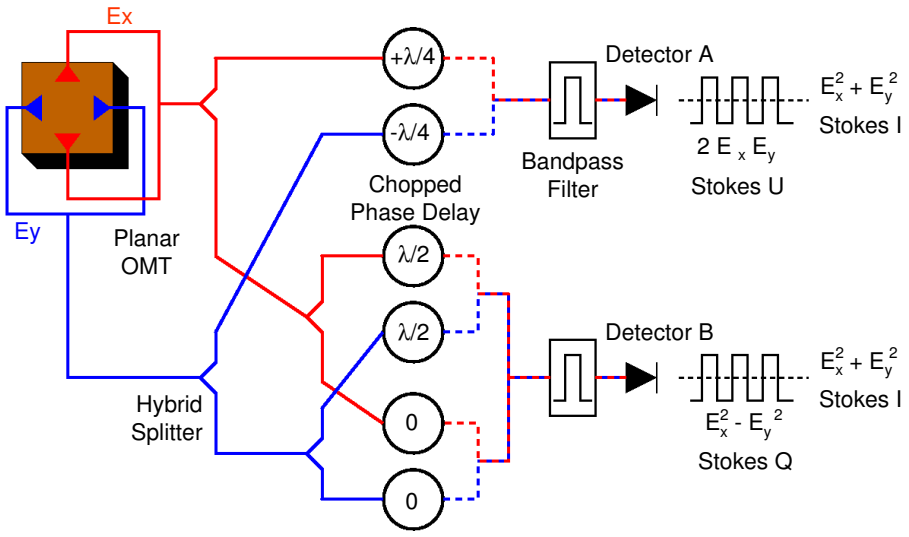

Figure 18. Symmetric version of planar IQU polarimeter. Each leg has one switch to minimize differential loss.

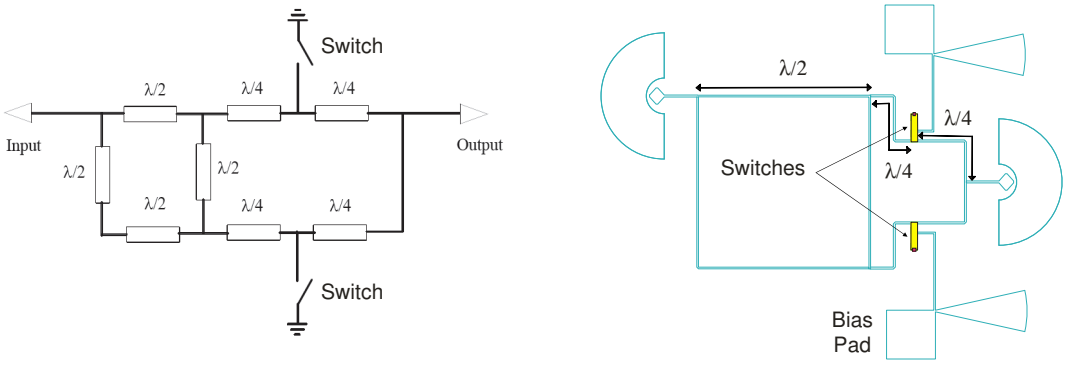

Figure 19. Broad-band phase circuit for CMB polarimetry. (left) Schematic representation. (right) Implementation at 3 mm wavelength.

Figure 19 shows a 90° phase shift circuit for CMB applications, along with a specific implementation of the circuit at 3mm wavelength. Figure 20 shows the predicted performance. Phase stability of a few degrees across a 30% bandpass is achievable. The insertion loss is low (typically 0.3 dB or better).

6.2.1. MEMS switches A planar polarimeter requires active switching. Micro Electro Mechanical Systems (MEMS) switches are one technology capable of operation at cryogenic temperatures and millimeter wavelengths. MEMS switches are miniature surface micromachined components providing controlled motion over a short distance to create either an open circuit or a short across a transmission line. Figure 21 shows a schematic switch for the PAPPA

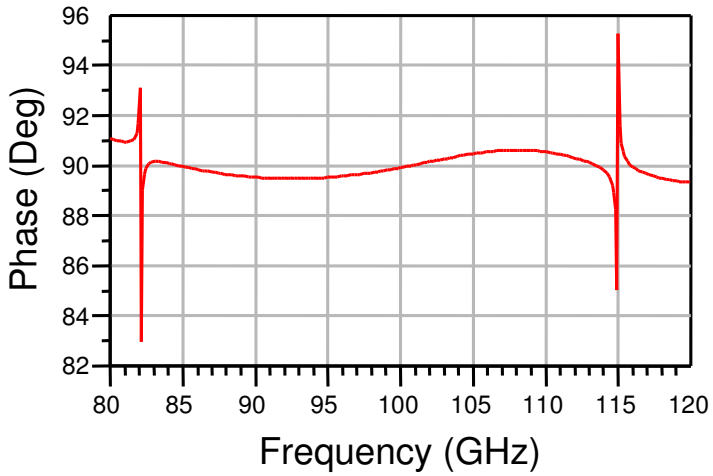

Figure 20. Calculated performance for the 90° phase circuit. Phase stability of a few degrees across a 30% bandpass is achievable.

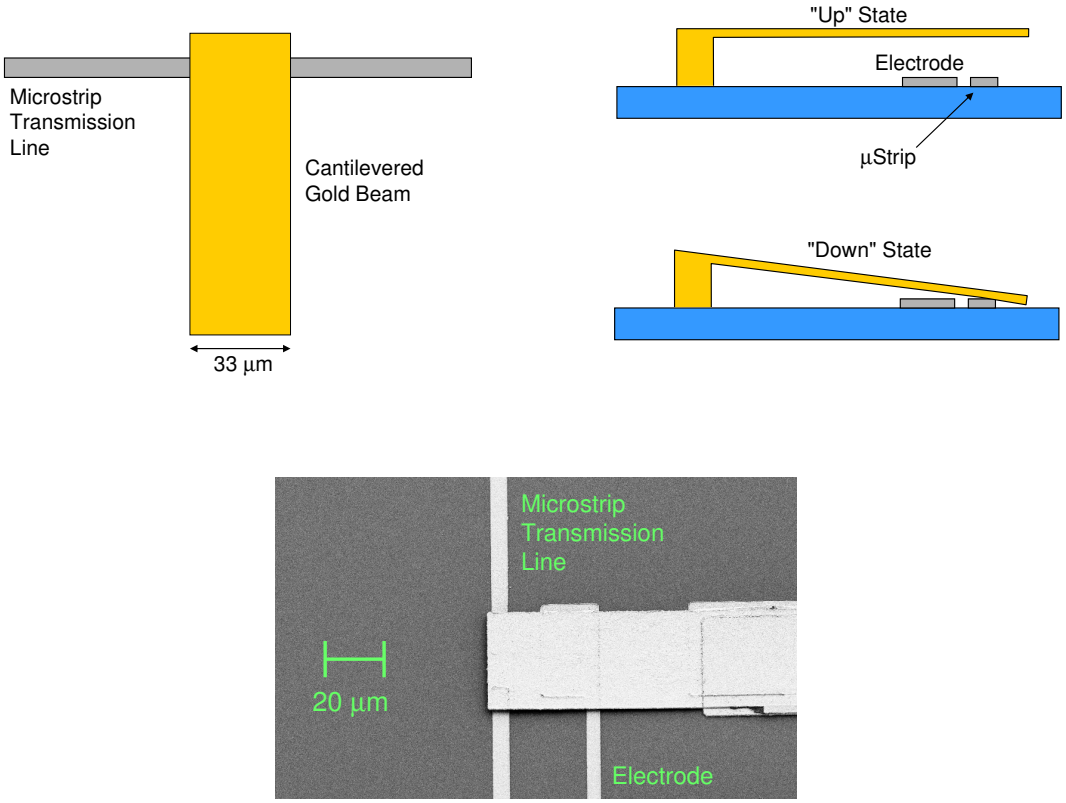

Figure 21. Schematic showing MEMS switch. (Top Left) Top view showing metal beam cantilevered above transmission line. (Top Right) Side view showing the beam in the "up" and "down" positions. (Bottom) Phase switches have reliably been fabricated using photolithographic techniques for operation at 3 mm wavelength.

polarimeter. It consists of a metal beam 33 μm $\times$ 100 μm $\times$ 1 μm thick cantilevered 1 μm above the transmission line. An electrostatic voltage applied to a pull-down electrode pulls the beam down to short out the transmission line. Other designs are possible, including non-contacting designs which modulate the capacitance between the cantilever and the transmission line.

MEMS switches are an attractive technology for CMB polarimetry. The switching transient time is small (a few μs) so that phase switching at kHz frequencies is possible. Commercial versions of RF-MEMS switches are available for frequencies up to approximately 20 GHz. Commercial MEMS switches operating at 1.5 K flew on the ARCADE suborbital mission. Prototype devices for operation at the higher frequencies typical for CMB polarization have been built at GSFC and the University of Virginia.

6.2.2. SIS switches Superconductor-Insulator-Superconductor (SIS) junctions can also be used as the switching element for a microcircuit modulator. Figure 22 shows performance of a prototype SIS switch developed at JPL. Efficiencies of order 80% have been demonstrated across a 15% fractional bandwidth at 3 mm wavelength.

6.3. Advantages and Disadvantages

Both MEMS and SIS switches share a number of advantages and disadvantages for use in CMB polarimetry. Advantages include the following:

- **Scalable Technology** The switches are produced using the same photolithographic techniques on the same wafer as the detectors, and are scalable to kilo-pixel focal plane arrays. No hand assembly is required to produce multiple copies of a "polarimeter-on-a-chip."
- **Fast Modulation** Switching speeds are inherently rapid (100 Hz or faster). The actual speed is likely to be limited by the power dissipation per switching cycle, since the total dissipation from all switches must not exceed the available cooling capacity.
- **Repeatability** Once the initial switch design is tested and verified, performance variability from one device to another should be small. This will reduce systematic effects associated with the overall circuit symmetry.
- **Cryogenic Reliability** There are no macroscopic moving parts (or for SIS switches, no moving parts at all), eliminating the risk associated with cryogenic mechanisms.

Disadvantages are dominated by the issue of complexity. Switch fabrication alone easily adds 10–20 steps (masking, deposition, etching, etc) to the photolithographic circuit production,

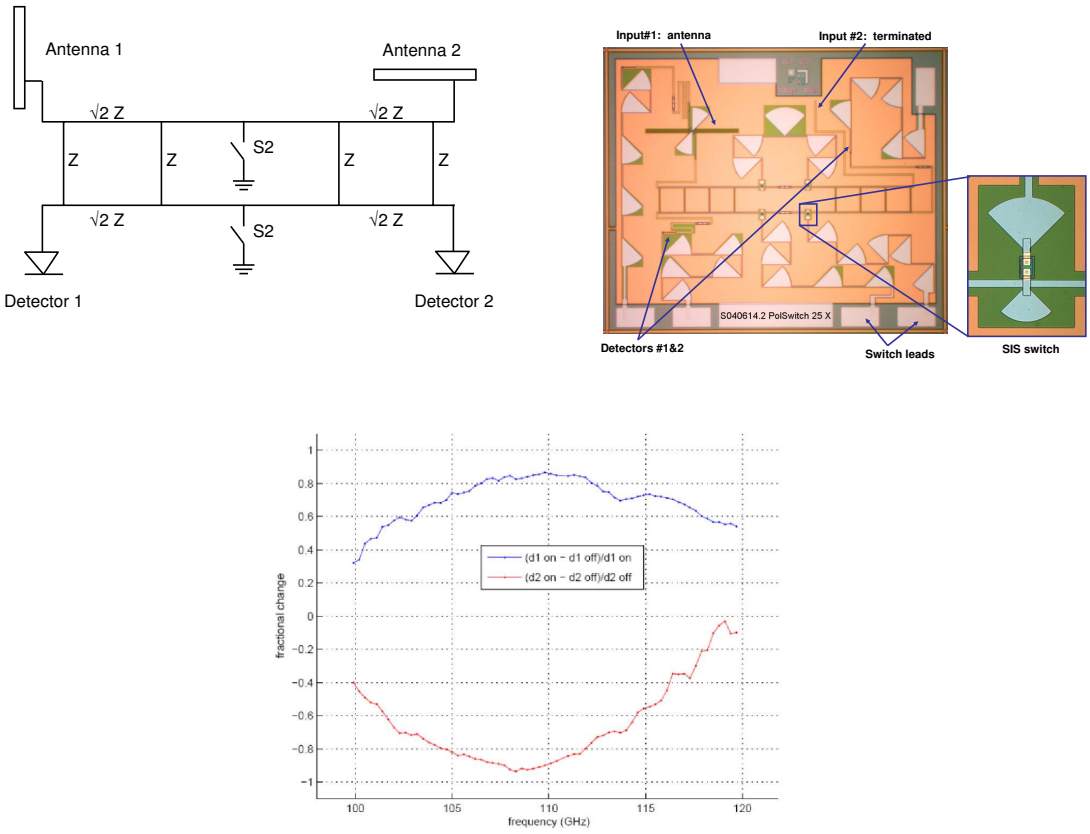

Figure 22. Demonstration of SIS switch. (Top Left) Circuit diagram for SIS test circuit. (Top Right) Photograph of fabricated circuit. (Bottom) Fractional signal modulation as the switches couple and decouple the detectors.

with resulting higher costs and lower yields. In addition, the circuit design necessary to achieve broad-band ($\Delta\nu/\nu \geq 0.15$) signal switching is complicated both for design and verification.

Largely due to the complications involved, these devices remain at low TRL. Phase-switched MEMS circuits have been demonstrated at GSFC and the University of Virginia, which retains a small program devoted to MEMS switch development. A prototype SIS switch has been demonstrated at JPL, but there is no longer an active program developing SIS switches. Both MEMS and SIS switches are currently at TRL $\sim$3.

Raising the modulators to TRL 5 would require 4 or more years development at funding levels roughly \$400K per year per project. Both the time and cost are dominated by the fixed costs associated with photolithographic fabrication for multi-mask processes. Testing costs are sub-dominant compared to fabrication.

Journal of Physics: Conference Series **155** (2009) 012006 doi:10.1088/1742-6596/155/1/012006

7. Millimeter Wave Orthomode Transducers

E J Wollack

Observational Cosmology Laboratory, NASA/GSFC, Greenbelt, MD 20771

E-mail: edward.j.wollack@nasa.gov

Abstract. An orthomode transducer (OMT) is a polarization selective splitter or diplexer. The function of this device in an imaging system is to separate the incident radiation into its orthogonal polarization states. Symmetric waveguide OMT devices have found widespread usage in radioastronomy, communications, and metrology at microwave through millimeter wavelengths due to their demonstrated performance. In this paper, the current status of OMT architectures and their application in the measurement of the Cosmic Microwave Background polarization is summarized.

7.1. Introduction

The term orthomode transducer (OMT) is traditionally reserved in the microwave literature to describe a guided wave device which operates on the linear polarization basis. Radiation collected by an antenna structure enters the OMT structure via the dual-mode or main-arm waveguide port and is separated into its horizontal and vertical polarization components. Related waveguide variants which separate the incident radiation field into left and right circular polarization can also be realized. In waveguide this can be achieved though the use of a septum polarizer, however, a quarterwave-plate followed by an OMT can have larger bandwidth. Ideally, these polarization discrimination devices should not adversely impact the systems isolation, optical efficiency, or operational bandwidth. In addition, when used in an imaging array, the OMT structure should be compatible with device integration and facilitate realization of the required environment for the sensors end use.

The role of waveguide polarization diplexers can be illuminated by considering their function in the more general technological context. The OMT is used in a system to separate linearly polarized light into its horizontal and vertical components. In a quasi-optical system this polarization splitting function is traditionally performed by a wire grid. A plane wave incident on the polarizer is separated by reflection and transmission of its linearly polarized components. An orthogonal pair of linearly polarized aerials in free space plays a similar function; however, strictly speaking as a dual-mode waveguide component, the OMT, does not play a role in defining the systems angular response. Spurious modal generation by an antennas feed structure can adversely influence the antenna response and must be limited by design. The OMT structure may also serve as a transition between transmission line types and can be used as a means of conveniently integrating functionality. The fundamental difference between these examples is the underlying mode space or basis on which the ideal device operates. One approach to make a polarization sensitive sensor is by defining the angular resolution with an antenna, then separating the desired polarization states with an OMT, and finally detecting these signals. An OMT allows a clean separation of optical beam definition and mode coupling functions required to define the sensor response.

7.2. Symmetric Orthomode Junctions

Receiver systems for radioastronomy and other precision coherent detector applications have historically used waveguide based polarization discrimination components due to their performance, volume, and mass. In practice, it is possible to keep the polarization isolation small compared to that arising from the optical elements, realize a good coupling, and achieve low

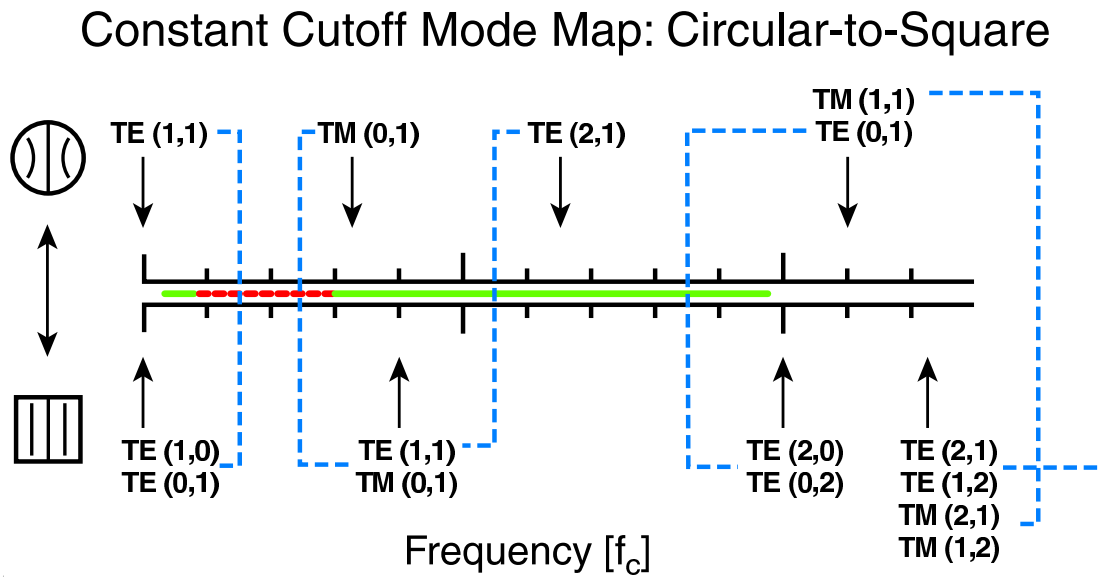

Figure 23. Circular and Square Waveguide Mode Map. The red line indicates the normalized frequency range available when the over-moded common-arm section is asymmetric with respect to rotation. The green line indicates the range available when the common-arm junction is symmetric. The blue dashed lines indicate self similar modal mappings between circular and square guide upon continuous deformation of their boundaries [67].

loss. Full waveguide bandwidth designs for cryogenic operation are known and are in relatively wide spread use. A key to achieving these properties is the use and understanding of symmetric feed and OMT structures.

The performance of all waveguide components are closely related to the underlying junction and electromagnetic symmetry in the structure [65],[66]. Asymmetric OMTs are commonly found in commercial microwave applications. The OMT main or common-arm port is coupled to dual-mode, typically circular or square, waveguide with the modes allowed by the structures symmetry. The bandwidth of asymmetric structures is limited in practice to a ∼10-20% fractional bandwidth by the excitation of higher-order modes. The underlying issue can be seen in the waveguide mode map for square and circular guide depicted in Figure 23. In an asymmetric structure the geometry has overlap and can excite modes in the desired pass band. To respond to this bandwidth reduction, a designer is driven to reduce the common-arm guide diameter which indirectly increases guide dispersion and loss. The use of symmetric OMTs enable the full >40% fractional bandwidth of the single-mode (horizontal and vertical polarization) ports to be used. This is achieved by limiting the excitation of higher-order modes in the dual-mode (common-arm) port structure.

In a symmetric OMT the polarization isolation is high and typically limited by residual misalignments. The co- and cross-polar responses are set by the design and realization of the beam-forming optics. The polarization isolation is defined as the leakage between the horizontal and vertical polarization ports. As such it is a scalar quantity. The cross-polarization on the other hand, is a measure of polarization response of the beam as a function of angle [68]. These terms can be found used interchangeably in the open literature; however, in general they describe fundamentally different properties. This distinction can provide valuable insight into the physical origin and can influence the control over systematic errors in polarimetric imaging systems.

The development of four-fold symmetric structures can be traced to the early work on turnstile

junctions by R. Dicke while at the MIT radiation laboratory. The waveguide turnstile junction is a natural candidate for wideband OMT performance as a result of its high symmetry; however, the devices inherent three-dimensional topology presents manufacturing challenges, complexity, and cost. Structures of this type are presently an area of active study for millimeter wavelength receiver applications [69]. The Robinson two-fold symmetric OMT used an orthogonal finline transition to pick off each polarization sequentially [70],[71]. An example of a four-fold symmetric adaptation of this approach is the quad-ridge OMT. By folding a part of the turnstile arms, Bifot [72],[73] was able to realize an OMT in a split-block configuration. A recent interesting variation on this design has been presented by Dunning [74],[75] which eliminates the need for the pins and septum used in the Bifot configuration. A more complete review of the historical development of symmetric OMT waveguide structures can be found in [66],[76],[77]. The historical development of these devices reveals a general trend toward reducing the number of components and assembly complexity while retaining the desired electromagnetic properties. These advances have enable realization and use of these structures to $\sim$1 mm.

We note that symmetric waveguide polarization diplexers have polarized outputs which topologically lie in orthogonal planes. For packaging most coherent receivers this does not pose a fundamental issue due to the existing chip fabrication, test and integration procedures, as well as number of receivers. As such, the structures described have been demonstrated and are suitable for use in CMB polarimetry in this context. However, large arrays of incoherent detectors require a higher level of integration than is practical with these inherently three-dimension waveguide structures. This has led to the investigation of planar topologies which allow on chip integration of the waveguide coupling structures and the sensors detectors. Several notable efforts to realize planar OMT junctions can provide useful insight to potential challenges. In avoiding the use of vias or crossovers, an OMT structure violating the desired four-fold symmetry was fabricated and realized an extremely narrow band response [78]. The symmetry of the structure is the key to controlling modal excitation and must be respected. A planar L-band OMT scale model prototype encountered relatively high power loss [79],[80],[81]. This issue was traced to coupling to dielectric substrate and loss in the power combiners. Recent innovations have enabled control over these design concerns and have greatly reduced the potential implementation risks with this approach [82],[83].

7.3. Technology Description

For incoherent polarization sensors having a single planar interface between the dual-mode waveguide port and the sensor chip, which contains a pair of detectors, is highly desirable. This allows a natural separation of items requiring tight photolithographic and loose mechanical tolerances in the integrated package. One approach to achieving this configuration is the use of a planar OMT with four-fold symmetry. The development efforts toward realizing OMT structures for incoherent detectors for use in characterization of the CMB polarization are briefly summarized.

The Clover instruments 97 GHz channel realizes its transition between the feed horns circular waveguide port and rectangular waveguide by using an electroformed turnstile junction OMT [84]. This design accepts a dual-mode circular waveguide inputs and then outputs the vertical and horizontal polarizations into single mode rectangular waveguide. The measured return loss is -20 dB and a polarization isolation of better than -40 dB. A finline transition is used between the waveguide and the 225 μm thick silicon substrate on which the detector resides. The silicon detector chip is mounted in E-plane split block rectangular waveguide. The edge of the chip is covered with metal serrations in the region where the chip is held in a groove in the block to prevent the formation of parasitic resonances in the final device response. The silicon chip has a tapered point to form an adiabatic transition from unloaded waveguide to waveguide loaded with silicon. Next, this mode is converted to antipodal finline and then to microstrip [85],[86]

before being terminated in the bolometers absorber.

For Clovers higher frequency channels (150 and 225 GHz) the OMT configuration will be a cylindrical waveguide with four-fold symmetric probes [87]. Signals from opposite probes will be combined in planar circuitry to form the vertical and horizontal polarizations that are connected directly to the TES detectors. This choice allows the OMT probes and TES detectors to reside on the same chip. Simulations have predicted a return loss of -20 dB and isolation of -60 dB. These predictions have been validated for scale models of the structure [88].

Goddard Space Flight Center is currently investigating polarimeter chips with four-fold symmetric probe antennas which transfer signals from the square waveguide to the microstrip lines. See Figure 24. These four-probe antennas are suspended on a thin silicon membrane. This approach uses superconducting niobium microstrip circuits to appropriately combine the desired modes. Broadband crossovers and terminations are used to symmetrize the microstrip lines. After combining, the signals are low-pass filtered and detected with a TES bolometer. The waveguide cut-off defines the lower edge of the operating band. Currently, the filter structure is under test in a custom cryogenic package using commercial microwave probes. A disordered metal alloy is used for the broadband terminations and loads. In this configuration, control over the chip-to-waveguide interface is an important consideration. In this design a photonic waveguide joint [82] with four-fold symmetry is used to prevent leakage of power from the waveguide into the volume of space in which the planar circuitry for the detectors reside. Appropriate attention to the details of the substrate and choke parameters allows control over coupling between the waveguide and the planar chip with the detectors and supporting circuitry. Full wave simulations indicate negligible insertion loss, high isolation and -20 dB return loss over greater than a 35% fractional bandwidth is achievable with this approach.

7.4. Planar OMT Benefits and Disadvantages

7.4.1. Benefits

- In a symmetric OMT the polarization isolation (leakage between the horizontal and vertical modes) is small and independent of the cross-polar response defined by the feed assembly. In operation, this consideration can be used to help in defining a system which limits the influence of spatial structure on the retrieved polarization signal.
- Elements requiring high tolerance are realized photolithographically and the remainder are realized by traditional machining techniques. This allows integration of planar band-pass filters, terminations, absorbers, and bias circuits required to tailor and define the detector response.
- The technology allows a natural partition between the beam-forming and detection circuitry which can be used for optimization of the system performance, characterization, and risk mitigation. The approach leverages existing fabrication approaches for fabrication of corrugated platelet feed horn arrays. Additional waveguide components (e.g., broadband waveplates [89],[90], active phase shifters or Faraday rotators [91], and filtering [92],[93]) can be accommodated in the sensor, if desired.
- The metal structures used in the feed array assembly can be used to support and shield the dielectrics used in the detectors. This design choice provides a natural path to achieving an environment for the sensor which is compatible with both the electromagnetic and ionizing radiation environments as well as providing thermal inertia to limit the impact of environmental changes on the instrument response.
- The detector chip resides in proximity to the antenna feed array interface. The use of a symmetric choke structure can be used to limit propagation of the signal and its sensitivity to the details of the gap geometry. This interface also can provide a convenient interface for a thermal break for the detectors.

- The planar OMT architecture is potentially compatible with, but does not require, modulators on the chip or in the dual-mode waveguide region of the assembly. As with all modulation approaches, the lowest level of complexity compatible with the required system performance and margin is advocated. In making such system level choices the risks associated with common and differing systematic effects need to be carefully considered in the context of how non-ideal responses, if present, will be mitigated. An answer to this the issue of how to appropriately partition the system such that systematic influences on the data are not degenerate presently remains open.

7.4.2. Disadvantages

- As with other approaches, throughput with illumination matched to optics ultimately links the number of sensors, resolution, and cost/risk. This places high importance on sensor performance, yield, and reliability to achieve science goals with acceptable margin.
- Mechanical alignment between mechanical interfaces must be achieved upon cooling.
- Focal plane area trade for beam quality leads to modest optical throughput.
- Planar OMT structures are presently at a low demonstrated level of technical readiness.

7.5. Technological Readiness Level

Conventional symmetric waveguide based orthomode junctions are presently at a relatively high level of technical readiness. They have been widely deployed in coherent millimeter wave systems for radioastronomy, however, a practical path toward the use of these three-dimensional structures in large scale arrays of bolometric detectors is lacking. Planar OMT structures compatible with usage in such arrays are presently under development. Scale models have been demonstrated and millimeter wave designs have been completed which are presently undergoing fabrication and test. As such, these devices are at relatively modest levels of technological readiness, somewhere in the range of $\sim$2-3, and will require additional investment to implement and deploy in systems.

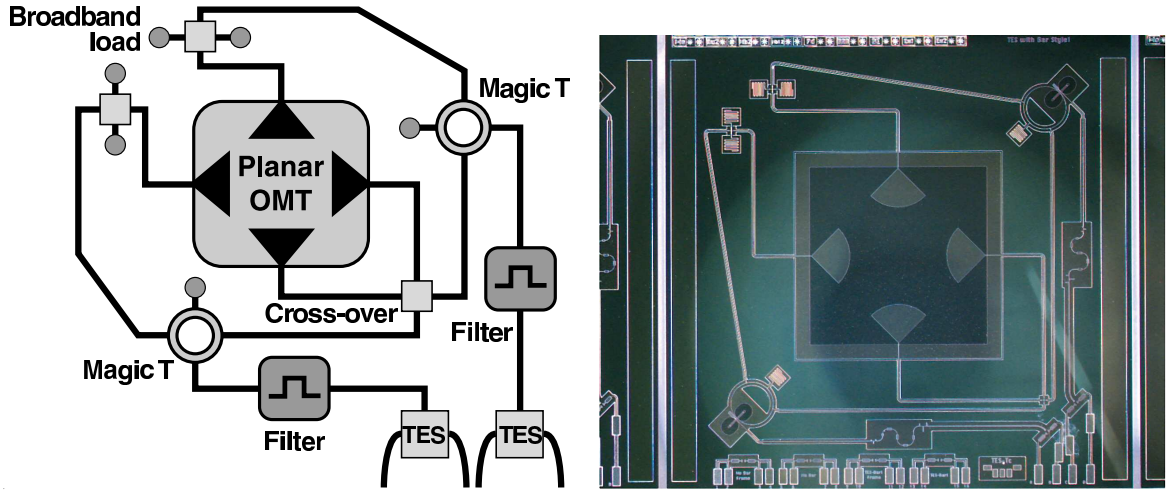

Figure 24. Symmetric OMT Circuit Diagram (Left) and Prototype Device (Right). In the implementation depicted the signals from a pair of waveguide probes are combined in the magic-T difference port. This enforces the desired symmetry and prevents excitation of the modes which can limit the desired response. An additional pair of crossovers has been added to symmetrise the phase between the vertical and horizontal OMT ports prior to filtering. An alternative implementation where the detector is differentially driven can be used if appropriate phase and amplitude matched filters can be achieved.

References

[1] Bock J, Church S, Devlin M, Hinshaw G, Lange A, Lee A, Page L, Partridge B, Ruhl J, Tegmark M, Timbie P, Weiss R, Winstein B and Zaldarriaga M 2006 *eprint arXiv:astro-ph/0604101*
[2] Montroy T E, Ade P A R, Bock J J, Bond J R, Borrill J, Boscaleri A, Cabella P, Contaldi C R, Crill B P, de Bernardis P, De Gasperis G, de Oliveira-Costa A, De Troia G, di Stefano G, Hivon E, Jaffe A H, Kisner T S, Jones W C, Lange A E, Masi S, Mauskopf P D, MacTavish C J, Melchiorri A, Natoli P, Netterfield C B, Pascale E, Piacentini F, Pogosyan D, Polenta G, Prunet S, Ricciardi S, Romeo G, Ruhl J E, Santini P, Tegmark M, Veneziani M and Vittorio N 2006 **647** 813–822 (*Preprint* `arXiv:astro-ph/0507514`)
[3] Hinderks J, Ade P, Bock J, Bowden M, Brown M L, Cahill G, Carlstrom J E, Castro P G, Church S, Culverhouse T, Friedman R, Ganga K, Gear W K, Gupta S, Harris J, Haynes V, Kovac J, Kirby E, Lange A E, Leitch E, Mallie O E, Melhuish S, Murphy A, Orlando A, Schwarz R, O' Sullivan C, Piccirillo L, Pryke C, Rajguru N, Rusholme B, Taylor A N, Thompson K L, Tucker C, Wu E Y S and Zemcov M 2008 *arXiv*
[4] Johnson B R, Collins J, Abroe M E, Ade P A R, Bock J, Borrill J, Boscaleri A, de Bernardis P, Hanany S, Jaffe A H, Jones T, Lee A T, Levinson L, Matsumura T, Rabii B, Renbarger T, Richards P L, Smoot G F, Stompor R, Tran H T, Winant C D, Wu J H P and Zuntz J 2007 **665** 42–54 (*Preprint* `arXiv:astro-ph/0611394`)
[5] Johnson B R, Collins J, Abroe M E, Ade P A R, Bock J, Borrill J, Boscaleri A, de Bernardis P, Hanany S, Jaffe A H, Jones T, Lee A T, Levinson L, Matsumura T, Rabii B, Renbarger T, Richards P L, Smoot G F, Stompor R, Tran H T, Winant C D, Wu J H P and Zuntz J 2007 **665** 42–54 (*Preprint* `arXiv:astro-ph/0611394`)
[6] Wu J H P, Zuntz J, Abroe M E, Ade P A R, Bock J, Borrill J, Collins J, Hanany S, Jaffe A H, Johnson B R, Jones T, Lee A T, Matsumura T, Rabii B, Renbarger T, Richards P L, Smoot G F, Stompor R, Tran H T and Winant C D 2007 **665** 55–66 (*Preprint* `arXiv:astro-ph/0611392`)
[7] Lau J M 2007 *CCAM: A Novel Millimeter-wave Instrument Using a Close-Packed TES Bolometer Array* Ph.D. thesis Princeton University
[8] Hecht E and Zajac A 1997 *Optics* (Addison Wesley)
[9] Savini G, Pisano G and Ade P A R 2006 *Applied Optics* **45(35)** 8907 – 8915
[10] Fowler J 2008 Personal communication
[11] Lee A 2008 Personal communication
[12] Pancharatnam S 1955 Achromatic combinations of birefringent plates Tech. Rep. 71 Raman Research

Institute, Bangalore 137-144
[13] Hanany S, Hubmayr J, Johnson B R, Matsumura T, Oxley P and Thibodeau M 2005 *Applied Optics* **44**(22) 4666–4670
[14] Pisano G, Savini G, Ade P A R, Haynes V and Gear W K 2006 *Applied Optics* **45**(27) 6982–6989
[15] Johnson B R, Abroe M E, Ade P, Bock J, Borrill J, Collins J S, Ferreira P, Hanany S, Jaffe A H, Jones T, Lee A T, Levinson L, Matsumura T, Rabii B, Renbarger T, Richards P L, Smoot G F, Stompor R, Tran H T and Winant C D 2003 *New Astronomy Review* **47** 1067–1075 astro-ph/0308259
[16] Rennick T S, Vaillancourt J E, Hildebrand R H and Heimsath S J 2002 *Proceedings of the 36th Aerospace Mechanisms Symposium*
[17] Hanany S, Matsumura T, Johnson B, Jones T, Hull R and Ma K B 2003 *IEEE Trans. Appl. Supercond.* **13** 2128–2133
[18] Oxley P, Ade P A, Baccigalupi C, deBernardis P, Cho H M, Devlin M J, Hanany S, Johnson B R, Jones T, Lee A T, Matsumura T, Miller A D, Milligan M, Renbarger T, Spieler H G, Stompor R, Tucker G S and Zaldarriaga M 2004 *Infrared Spaceborne Remote Sensing XII* (*Presented at the Society of Photo-Optical Instrumentation Engineers (SPIE) Conference* vol 5543) ed Strojnik M pp 320–331
[19] Hanany S 2008 Personal communication
[20] Keating B G, O'Dell C W, Gundersen J O, Piccirillo L, Stebor N C and Timbie P T 2003 *Astrophysical Journal Supplement Series* **144** 1–20
[21] Yoon K W, Ade P A R, Barkats D, Battle J O, Bierman E M, Bock J J, Brevik J A, Chiang H C, Crites A, Dowell C D, Duband L, Griffin G S, Hivon E F, Holzapfel W L, Hristov V V, Keating B G, Kovac J M, Kuo C L, Lange A E, Leitch E M, Mason P V, Nguyen H T, Ponthieu N, Takahashi Y D, Renbarger T, Weintraub L C and Woolsey D 2006 *Millimeter and Submillimeter Detectors and Instrumentation for Astronomy III* (*Presented at the Society of Photo-Optical Instrumentation Engineers (SPIE) Conference* vol 6275) ed Zmuidzinas J, Holland W S, Withington S and Duncan W
[22] Leitch E M, Kovac J M, Pryke C, Carlstrom J E, Halverson N W, Holzapfel W L, Dragovan M, Reddall B and Sandberg E S 2002 *Nature* **420** 763–771
[23] Caderni N, Fabbri R, Melchiorri B, Melchiorri F and Natale V 1978 **17** 1908–1918 URL `http://adsabs.harvard.edu/cgi-bin/nph-bib_query?bibcode=1978PhRvD..17.1908Cdb_key=AST`
[24] Murray A G, Flett A M, Murray G and Ade P A R 1992 *Infrared Physics* **33** 113–125
[25] Hildebrand R H, Davidson J A, Dotson J L, Dowell C D, Novak G and Vaillancourt J E 2000 **112** 1215–1235 URL `http://adsabs.harvard.edu/cgi-bin/nph-bib_query?bibcode=2000PASP..112.1215Hdb_key=AST`
[26] Lubin P M and Smoot G F 1979 *Physical Review Letters* **42** 129–132 URL `http://adsabs.harvard.edu/cgi-bin/nph-bib_query?bibcode=1979PhRvL..42..129Ldb_key=AST`
[27] Keating B G, Ade P A R, Bock J J, Hivon E, Holzapfel W L, Lange A E, Nguyen H and Yoon K 2003 *Polarimetry in Astronomy. Edited by Silvano Fineschi. Proceedings of the SPIE, Volume 4843.* pp 284–295
[28] Timbie P and Tucker G 2008 *this volume*
[29] Nanos G P 1979 **232** 341–347 URL `http://adsabs.harvard.edu/cgi-bin/nph-bib_query?bibcode=1979ApJ...232..341Ndb_key=AST`
[30] Barnes C E 1961 *IEEE Trans. Microwave Theory Tech.* **9** 519
[31] Erickson N R 2001 *IEEE Trans. Microwave Theory Tech.* **1** 1
[32] Jones W C, Bhatia R, Bock J J and Lange A E 2003 *Millimeter and Submillimeter Detectors for Astronomy* vol 4855 ed Phillips T G and Zmuidzinas J pp 227–238
[33] Nanos G P J 1974 *Ph.D. Thesis*
[34] Page L, Hinshaw G, Komatsu E, Nolta M R, Spergel D N, Bennett C L, Barnes C, Bean R, Doré O, Dunkley J, Halpern M, Hill R S, Jarosik N, Kogut A, Limon M, Meyer S S, Odegard N, Peiris H V, Tucker G S, Verde L, Weiland J L, Wollack E and Wright E L 2007 *Ap. J. Supp. Ser.* **170** 335–376 (*Preprint* `arXiv:astro-ph/0603450`)
[35] Martin D and Puplett E 1970 *Infrared Physics* **10** 105–109
[36] Mather J C, Fixsen D J and Shafer R A 1993 *Proc. SPIE Vol. 2019, p. 168-179, Infrared Spaceborne Remote Sensing, Marija S. Scholl; Ed.* (*Presented at the Society of Photo-Optical Instrumentation Engineers (SPIE) Conference* vol 2019) ed Scholl M S pp 168–179
[37] Martin D 1974 *Infrared and Millimeter Waves* vol 6 ed Button J (Academic Press)
[38] Battistelli E, DePetris M, Lamagna L, Maoli R, Melchiorri F, Palladino E and Savini G 2002 *astro-ph/0209180v1*
[39] Catalano A, Conversi L, de Gregori S, de Petris M, Lamagna L, Maoli R, Savini G, Battistelli E S and Orlando A 2004 *New Astronomy* **10** 79–89 (*Preprint* `arXiv:astro-ph/0405399`)
[40] Howard J, Peebles W and NC Luhmann J 1986 *IJIMW* **7** 1591–1603
[41] Houde M, Akeson R L, Carlstrom J E, Lamb J W, Schleuning D A and Woody D P 2001 *PASP* **113** 622–638

(*Preprint* arXiv:astro-ph/0311414)
[42] Akeson R L, Carlstrom J E, Phillips J A and Woody D P 1996 *ApJL* **456** L45+
[43] Erickson N 1978 *IEEE MTT-S Intl. Microwave Symposium Digest* 438–439
[44] Manabe T, Inatani J, Murk A, Wylde R J, Seta M and Martin D H 2003 *IEEE Transactions on Microwave Theory and Techniques* **51** 1696–1704
[45] Erickson N 1987 *IJIMW* **8** 1015–1025
[46] Krejny M, Chuss D, Drouet d'Aubigny C, Golish D, Houde M, Hui H, Kulesa C, Loewenstein R F, Moseley S H, Novak G, Voellmer G, Walker C and Wollack E 2008 *Applied Optics* **in press** (*Preprint* 0803.3759)
[47] Chuss D T, Wollack E J, Moseley S H and Novak G 2006 *Applied Optics* **45** 5107–5117
[48] Lubin P 2005 *Private Communication*
[49] Leonardi R, Williams B, Bersanelli M, Ferreira I, Lubin P M, Meinhold P R, O'Neill H, Stebor N C, Villa F, Villela T and Wuensche C A 2006 *New Astronomy Review* **50** 977–983
[50] Shinnaga H, Tsuboi M and Kasuga T 1999 *PASJ* **51** 175–184
[51] Siringo G, Kreysa E, Reichertz L A and Menten K M 2004 *Astronomy and Astrophysics* **422** 751–760
[52] Chuss D and Wollack E 2008 *In preparation*
[53] Staguhn J G, Benford D J, Pajot F, Ames T, Allen C A, Chervenak J A, Lefranc S, Maher S, Moseley Jr S H, Phillips T, Rioux C G, Shafer R A and Voellmer G M *Millimeter and Submillimeter Detectors for Astronomy II*
[54] Bradford C M, Stacey G J, Swain M R, Nikola T, Bolatto A D, Jackson J M, Savage M L, Davidson J A and Ade P A R 2002 *Applied Optics* **41** 2561–2574 (*Preprint* arXiv:astro-ph/0205159)
[55] Voellmer G M, Chuss D T, Jackson M, Krejny M, Moseley S H, Novak G and Wollack E J 2006 *Optomechanical Technologies for Astronomy. Edited by Atad-Ettedgui, Eli; Antebi, Joseph; Lemke, Dietrich. Proceedings of the SPIE, Volume 6273, pp. 62733P (2006).* (*Presented at the Society of Photo-Optical Instrumentation Engineers (SPIE) Conference* vol 6273)
[56] Lahtinen J and Halilikainen M 1999 *IJIMW* **20** 3
[57] Novak G, Sundwall J L and Pernic R J 1989 *Applied Optics* **28** 3425–3427
[58] Voellmer G M, Bennett C L, Chuss D T, Eimer J, Hui H, Moseley S H, Novak G, Wollack E J and Zeng L 2008 *in preparation* Presented at the Society of Photo-Optical Instrumentation Engineers (SPIE) Conference
[59] Pisano G, Savini G and Ade P A R 2008 *Applied Optics* 6251–6256
[60] Pisano G, Savini G, Ade P A R, Haynes V and Gear W K 2006 *Applied Optics* **45** 6982–89
[61] Savini G, Pisano G and Ade P A R 2006 *Applied Optics* **45** 8907–15
[62] Pancharatnam S 1955 *Proceeding of Indian Academy of Sciences* **41** 137–44
[63] Shatrow A, Chuprin A and Sivov A 1995 *IEEE Trans. Ant. Prop.* **43** 109–13
[64] Ulrich R 1967 *Infrared Physics* **7** 37–55
[65] Montgomery C G, Dicke R H and Purcell E M 1948 *MIT Radiation Laboratory Series* vol 8 (New York: McGraw-Hill) chap 12
[66] Uher J, Bornemann J and Rosenberg U 1993 *Waveguide components for Antenna Feed Systems: Theory and CAD* (Norwood, MA: Artech House)
[67] Thompson D W 1917 *On Growth and Form* (Cambridge: Cambridge University Press)
[68] Ludwig A C 1973 *IEEE Transactions on Antennas and Propagation* **21** 116–119
[69] Navarrini A and Plambeck R 2006 *IEEE Transactions on Microwave Theory and Techniques* **54** 272–277
[70] Robertson S D 1956 *IRE Transactions on Microwave Theory Techniques* **4** 263–267
[71] Chattopadhyay G and Carlstrom J 1999 *IEEE Microwave and Guided Wave Letters* **9** 339 – 341
[72] Bifot A M, Lier E and Schaug-Pettersen T 1990 *Proceedings of the IEEE* **137** 396400
[73] Bifot A M 1991 *European Transactions on Telecommunications and Related Technologies* **2** 503 – 510
[74] Dunning A 2002 *Workshop on the Applications of Radio Science*
[75] Moorey G e a 2006 *Radioastronomy Proceedings Applications of Radio Science Conference*
[76] Wollack E 1996 *NRAO EDIR Memo Series*
[77] Wollack E and Grammer W 2003 *Proceedings of the 14th International Symposium on Space TeraHertz Technology in Tucson, AZ* 169–176
[78] Jackson R W 2001 *IEEE Microwave and Wireless Components* **11**
[79] Bock D 1999 *BIMA Memo #74 Letters* **11** 483–485
[80] Engargiola G and Plambeck R L 2002 *BIMA Memo #87*
[81] Engargiola G and Plambeck R L 2003 *Review of Scientific Instruments* **74** 1380 – 1382
[82] Hesler J 2001 *IEEE-MTT-S International Microwave Symposium Digest* **2** 783–786
[83] U-yen K, Wollack E J, Papapolymerou J and Laskar J 2008 *IEEE Transactions on Microwave Theory and Techniques* **56** 172–177
[84] Pisano G, Pietranera L, Isaak K, Piccirillo L, Johnson B R, Maffei B and Melhuish S 2007 *IEEE Microwave and Wireless Components Letters* **17** 286288

[85] North C E, Yassin G and Grimes P K 2006 *Proceedings of the 17th International Symposium. on Space Terahertz Technology*
[86] Yassin G, Withington S, Buffey M, Jacobs K and Wulff S 2000 *IEEE Transactions on Microwave Theory and Techniques* **48** 662
[87] Grimes P K, King O G, Yassin G and Jones M E 2007 *Electronics Letters* **43**
[88] North C E *et al.* 2007 *18th Int. Symp. on Space Terahertz Technology*
[89] Kovac J M 2003 *Detection of Polarization in the Cosmic Microwave Background using DASI* Ph.D. thesis University of Chicago, Chicago, IL
[90] Kovac J M and Carlstrom J E 2005 Broadband high precision circular polarizers and retarders in waveguides US patent number 6963253
[91] Keating B G 2008 Faraday rotation modulators published in these proceedings.
[92] Amari S and Bornemann J 2001 *Microwave and Optical Technology Letters* **31** 334336
[93] Vanin F M *et al.* 2006 *IEEE MTT-S International Microwave Symposium Digest* 127130